FINAL TECHNICAL REPORT

on

NASA GRANT NO. NGR 05-020-644

HIGH RESOLUTION OBSERVATIONS OF JOVIAN MAGNETOSPHERIC MICROWAVE SYNCHROTRON EMISSION

by

L.R. D'Addario and S.J. Wernecke

June 1974

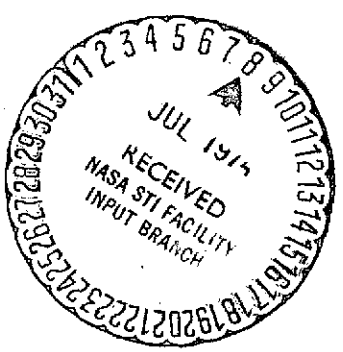

TABLE OF CONTENTS

1. INTRODUCTION AND SUMMARY

1.1. CHARACTER OF JUPITER'S MICROWAVE EMISSIONS

The microwave radiation from Jupiter has been studied over a wide range of wavelengths (e.g., Dickel et al. 1970), and has been found to arise from both thermal and non-thermal mechanisms. At the longer wavelengths (~10 to 20 cm), most of the flux is due to synchrotron radiation from relativistic electrons trapped in the planet's magnetic field. The source of these electrons and the mechanism for their acceleration to relativistic energies have been investigated theoretically (e.g. Brice and McDonough 1973), but the absence of definitive measurements of their distribution has prevented observational confirmation of the results.

As one moves toward shorter wavelengths, the synchrotron flux remains approximately constant, but the thermal contribution becomes increasingly important. Below about 4 cm, the latter contributes most of the flux; it is presumed to originate in the upper atmosphere of the planet. Supposing the radiation to come from a uniformly bright disk of the optical diameter, the observations are consistent with a constant brightness temperature of about 140 K for wavelengths from 1 cm to the infrared. Between 1 cm and 10 cm, the brightness temperature of the disk (after correcting for the synchrotron flux) appears to increase somewhat, to perhaps 250 K, possibly due to penetration to a deeper level in the atmosphere.

Ground-based observations of Jupiter at centimeter wavelengths are thus useful for studying (1) the temperature of the upper atmosphere; (2) the structure of the magnetic field; and (3) the distribution of

relativistic electrons. Of course, other quantities can be studied indirectly via appropriate models. With respect to the magnetosphere, it should be noted that only those portions significantly populated with relativistic electrons are directly accessible to radio observations.

The following important properties of the centimeter-wavelength radiation were established during the 1960's (for an excellent review of work through 1968, see Carr and Gulkis 1969). The non-thermal component is strongly linearly polarized, with the plane of polarization rocking $\pm 10^{\circ}$ in synchronism with the planet's rotation. There is also a small amount of circular polarization. The spectrum is nearly flat from 200 to 3000 MHz, with an average flux density of 6.7 f.u.[1] It has usually been supposed that the synchrotron spectrum remains flat to much higher frequencies also (Dickel et al. 1970), but unambiguous separation of the thermal disk is difficult.

Observations with high angular resolution, using synthesis telescopes, have been made at 1.4 GHz (Branson 1968) and 2.9 GHz (Berge 1966). These showed that the peak synchrotron emission at those frequencies occurs about 1.8 R_J from Jupiter's center, where R_J is the equatorial radius of the planet. Since the time of these studies, there has apparently been little high-resolution work reported, perhaps because the rapid rotation of Jupiter complicates the usual earth-rotation synthesis techniques.

1.2. PIONEER 10

The recent Pioneer 10 flyby of Jupiter has in some respects provided us with a much more detailed knowledge of the magnetosphere than had been

---

[1] 1.0 flux unit (f.u.) = 10^{-26} W m^{-2} Hz^{-1}.

possible from ground-based observations. All of our former information came from the radio observations, which give no direct information about the outer magnetosphere or about the distribution of protons or low-energy electrons. However, our extensive knowledge of the Earth's magnetosphere has been a useful guide to what might be expected on Jupiter (Brice and Ioannidis 1970, Warwick 1970).

At periapsis, Pioneer 10 passed $2.85R_J$ from Jupiter's center, outside the region of maximum synchrotron radiation. Thus, particle density data from the spacecraft is complementary to that deducible from the radio observations. Pioneer 10 also provided the first direct magnetic field measurements (Smith et al. 1974); inside about $6R_J$ the field appears dipolar with moment $4.0R_J^3$ gauss and a 15° tilt with respect to the rotation axis. The latter is in apparent disagreement with the 10 cm polarization rocking of $\pm 10^\circ$ (Klein and Gulkis 1974).

1.3. THE PRESENT STUDY

The work which we report here is intended to add significantly to the available high-resolution radio observations of Jupiter. We have used the Stanford synthesis telescope to observe the planet over an extended period of time during 1973, beginning in May and continuing through the Pioneer 10 encounter in December.

The telescope is a five-element, minimum redundancy, east-west array, which results in the simultaneous availability of nine different interferometer baselines. It allows, in principle, instantaneous synthesis of strip scans of the source brightness, and in practice such scans can be produced

every few minutes for sources of Jupiter's strength (15-20 f.u.). Therefore, we have the possibility of easily obtaining the high time resolution needed to account for Jupiter's rapid rotation, simultaneously with good spatial resolution. (It should be noted that the instantaneous spatial resolution is one-dimensional, so that in general two-dimensional mapping requires extended observations utilizing earth rotation. At Jupiter's declination during 1973, -20°, the tracking range was such that all scans were within 11° of east-west on the sky.) The equivalent half-power beamwidth of these scans is $\sim 20''$, and our experience shows that this allows positions and widths of sources to be measured to a precision of $\sim 1''$.

The telescope operates at 10.69 GHz (2.80 cm wavelength), where the radiation from Jupiter is predominately thermal. In order to study the magnetosphere, it was necessary to separate this thermal radiation from the synchrotron radiation. The strength, size and location of the latter were largely unknown at this frequency, but we anticipated that if it amounted to only a few flux units it would be easily detectable (receiver noise was 0.25 f.u. for each interferometer in 16^{m} of integrating time). The separation can be accomplished using the spatial resolution of the instrument, provided that most of the relativisitic electrons are concentrated away from the thermal disk; certainly concentrations at $1.8R_{J}$ would be resolvable, if only they emit sufficient flux. Separation can also be accomplished by using properties of the synchrotron radiation itself, such as its polarization and beaming in the magnetic equatorial plane. Both methods were used in our analysis (Section 4). As it turned out, small calibration errors made the separation quite difficult, for

reasons which we shall consider in detail later. We can nevertheless conclude that the synchrotron flux at 10 GHz must be considerably smaller than at lower frequencies, so that the spectrum does not remain flat.

We have also studied the thermal disk radiation in a search for limb darkening or brightening. No significant effects of this kind were seen, the best fit disk being always very close to the optical radius. We deduce a constant disk brightness temperature of 160 ±10 K at 2.8 cm, in reasonable agreement with reported single antenna measurements at surrounding wavelengths.

A final objective of our study was to look for time variations in observations made simultaneously with the Pioneer 10 encounter, and to correlate these with spacecraft observations. We were not able to find any significant variations, although it should be kept in mind that any variable radiation we might have observed is likely to have originated from a region of the magnetosphere closer to Jupiter than periapsis.

In what follows, we give a detailed discussion of the observations, their analysis, and the results.

2. TELESCOPE PARAMETERS AND CALIBRATION

2.1. HARDWARE

The Stanford synthesis telescope includes five 18.6 m diameter paraboloids on polar mounts, arranged in a linear minimum-redundancy array (Moffett 1968) along a baseline which is very nearly east-west. Each pair of antennas is connected to form a multiplying interferometer. Nine baselines are thus simultaneously sampled, their lengths being 22.8n meters, n = 1,2,...,9. Using earth-rotation synthesis (Ryle 1962), measurements of the two-dimensional Fourier transform of the brightness distribution of a celestial source may be obtained.

Details of the design, construction and operation of the instrument have been given elsewhere (Bracewell et al. 1973), and will not be dwelt upon here; we shall discuss only those points which are particularly relevant to the Jupiter observations. Major parameters of the telescope[2] are given in Table 1.

Table 1

TELESCOPE PARAMETERS DURING JUPITER OBSERVATIONS

Observing frequency	10,690 MHz (λ = 2.800 cm)
Baseline interval	815.1 λ
Maximum baseline	7336 λ
Equivalent half-power beamwidth, instantaneous, uniform weighting, hour angle = 0	$18.1''$
Tracking range declination > 20^{o}	$\pm 5.0^{h}$
declination = -20^{o}	$\pm 2.1^{h}$
Receiver noise temperature, each antenna	1000 K
Integrating time for 1.0 f.u. r.m.s. complex visibility, each interferometer	1^{m}
Polarization	linear, E-vector north-south

[2] These are the values which were in effect during the Jupiter observations; some of them, particularly the receiver noise temperatures, have since been greatly improved.

2.2. COVERAGE

During all of 1973, Jupiter's declination was near -20^{o}. At this declination the array can track a source for 4.2^{h}, resulting in the spatial-frequency plane (Fourier transform plane) coverage shown in Fig. 1. The coordinates u and v are in the directions west and north, respectively, on the local sky. It should be apparent that most of the available resolution is in the east-west direction. Also plotted for comparison are three vectors representing spatial frequencies of magnitude $(80'')^{-1}$ = 2630 rad^{-1} ($80'' \approx 4R_J$) and directions parallel to Jupiter's equator (whose position angle remained essentially constant over the period of the observations) and parallel to Jupiter's magnetic equator in its extreme positions; to calculate the latter we have assumed an angle of 15^{o} between the rotation axis and magnetic dipole moment (Smith et al. 1974).

Linearly-polarized feed horns with the electric vector oriented north-south were used throughout the observations. This polarization is nearly parallel to the magnetic dipole moment at one extreme of the dipole's rocking.

2.3. CALIBRATION

The raw output of the instrument consists of estimates of the complex correlation of the signals from each antenna pair, averaged over an adjustable integrating period (for the present observations, the integrating time was slightly over 5^{m}), and continuously correcting for apparent source motion (fringe rotation). The estimates are produced by an on-line computer from samples of the outputs of analog multipliers. Thus, at the end of each integrating period ten complex numbers are

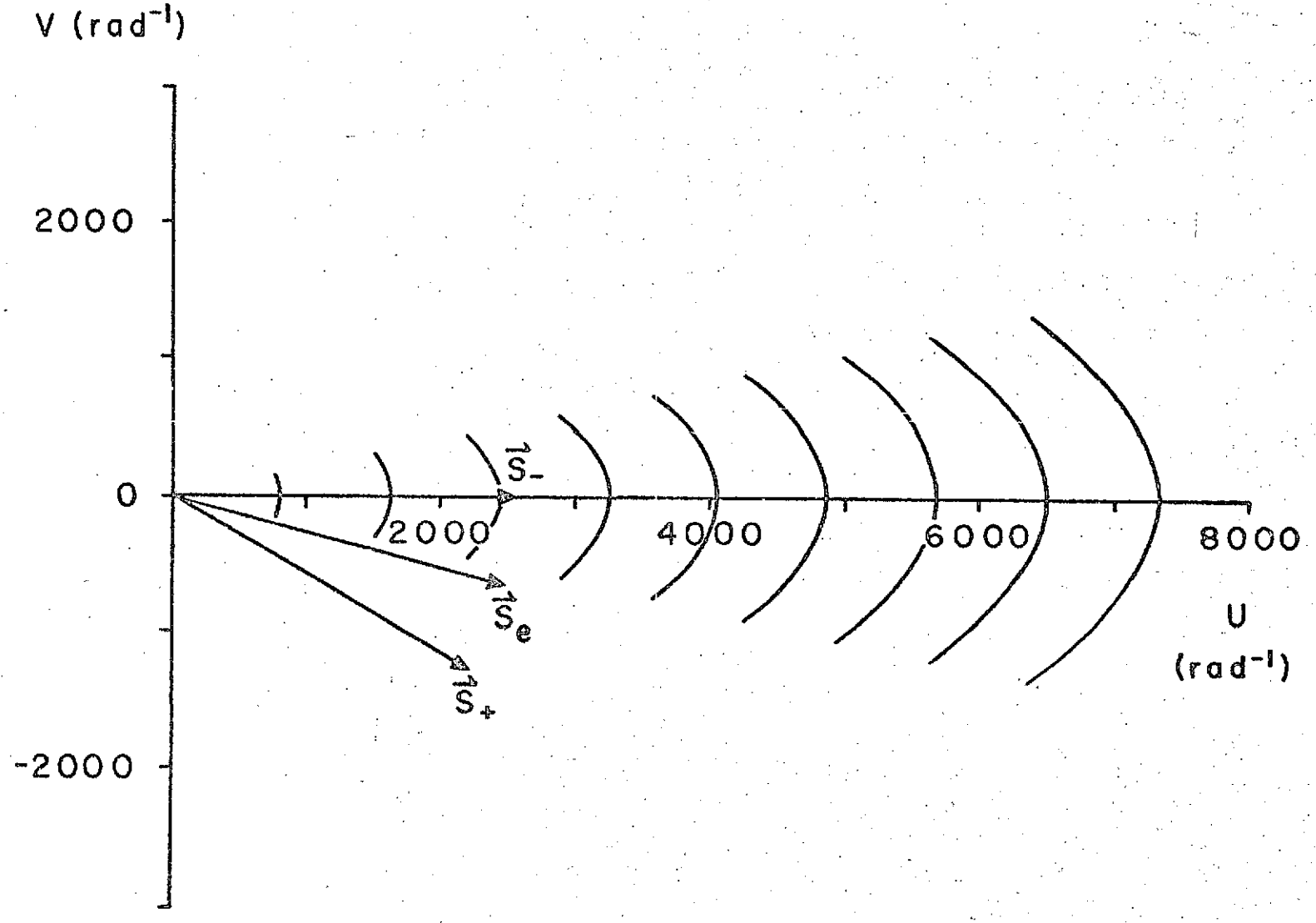

FIG. 1. Spatial frequency plane coverage of the Stanford telescope at Jupiter's declination during 1973 (-20°), indicated by the solid curves. The vector $\vec{s}_e$ is parallel to Jupiter's rotational equator; $\vec{s}_+$ and $\vec{s}_-$ are approximately parallel to Jupiter's magnetic equator at its extreme orientations. $\vec{s}_e$, $\vec{s}_+$, $\vec{s}_-$ have magnitudes of $(80'')^{-1} \approx (4\ R_J)^{-1}$.

available (one for each interferometer, with one redundant baseline); these are recorded on magnetic tape for off-line analysis.

Dividing each raw correlation by the complex gain of the corresponding interferometer channel converts it to a "calibrated" complex visibility (unnormalized), usually expressed in flux units. The complex gains are determined from observations of one or more calibration sources (unresolved sources of known position and flux density) at about the same time as the observation of an unknown source.

To minimize the frequency with which such calibration sources need to be observed, most of the variation in complex gains attributable to the receiver electronics is monitored by direct measurements, and removed in an early stage of the data reduction. Two quantities are measured: the power gain through each receiver is determined by injecting a known amount of broadband noise, and the electrical lengths of the transmission lines used to distribute the local oscillator reference signal are determined by a modulated reflector and synchronous phase detector (for details, see Bracewell et al. 1973).

Calibration of the pointing of the individual antennas and of the phase function of each interferometer (the latter consisting principally of an accurate determination of the vector baseline) were carried out over the whole visible sky in programs separate from the Jupiter observations (Price 1973; Wernecke 1973). A large number of calibration sources was observed and least-squares fits of model functions were obtained, giving r.m.s. residuals of about $30''$ for the pointing and $.01\lambda$ for the phase. However, prior to the 18-day observing program (see Section 3), we performed a specific check of pointing residuals near Jupiter's declination and discovered residuals $\sim 1'$ in two antennas; appropriate corrections were applied in

subsequent observations. These pointing errors should be compared with the single-antenna half-power beamwidth, which is $7'$; note also that we expect significant brightness only from a region of width approximately $4\ R_J \approx 80''$.

3. THE OBSERVING PROGRAM

As noted earlier, the major component of radiation received from Jupiter at 2.8 cm is of thermal origin, and studies at lower frequencies (Branson 1968, Berge 1966) have shown that synchrotron emission from the magnetosphere is maximum at a distance of about $1.8R_J$ from the planet's center. Thus, we considered that the resolution of the Stanford array might be used to separate the synchrotron component from the disk's thermal emission. Preliminary observations made early in 1973 indicated that less than 10% of the total flux received might be attributed to synchrotron emission. These results were useful in determining subsequent observing strategy.

All observations were made with linearly polarized feeds with a north-south electric field vector orientation. During each observation receiver gains and local oscillator line lengths were measured at intervals of 1 hour and 1/2 hour, respectively. Calibration sources used in the Jupiter observations were 3C345 at 40 degrees declination and PKS 2134+00 at 0 degrees declination. 3C345 and PKS 2134+00 have flux densities of approximately 12.0 and 10.5 f.u. The position angle of Jupiter's rotation axis was approximately 344 degrees in the latter half of 1973; consequently, the position angle of the interferometer baseline with respect to Jupiter's rotational equator varied from about 4 degrees to 28 degrees during each day's tracking (see Fig. 1). Because of this limited rotation, high resolution is obtained

only in one direction, and meaningful two-dimensional brightness maps cannot be synthesized.

Three major observing programs were executed:

1. Weekly observations: To study long term effects, we made weekly observations of Jupiter at meridian crossing for four months between May 4 and September 23. In each observation we tracked Jupiter for 30-60 minutes and included 30 minutes on PKS 2134+00 for calibration. During the four month period, the angular diameter of the optical disk grew from 37 arcsec to 45 arcsec; if the disk brightness temperature at 2.8 cm were 140 K (the infrared value), the corresponding flux density increase would have been from 12.5 to 18.6 f.u.

2. Daily observations: To permit study of any changes of Jupiter's appearance with central meridian longitude (CML), we observed Jupiter for eighteen consecutive days during the period 15 October to 1 November 1973, except for 22 October, when adverse weather conditions prevented observations. Jupiter was tracked for four hours each day. For calibration we tracked 3C345 for 30 minutes before observing Jupiter, PKS 2134+00 for 20 minutes after Jupiter crossed the meridian and again for 30 minutes at the end of the observing session. At the end of this eighteen day period we also tracked PKS 0834-20 to provide a check of the calibration of the telescope's response at Jupiter's declination.

3. Fly-by observations: To allow correlation of ground-based observations with Pioneer 10 measurements, Jupiter was tracked for four hours each day for the four days surrounding periapsis. Calibration was accomplished with 30 minutes tracking of 3C345 before tracking Jupiter and 30 minutes of PKS 2134+00 at the end of the observation.

In Figures 2 and 3 we summarize the dates of the observations and plot the Jovian central meridian longitude[3] variation during each day's run. It can be seen that the daily observations provide fairly complete CML coverage. The time of Pioneer 10 periapsis is also indicated.

4. DATA ANALYSIS

4.1. PRELIMINARY REDUCTION

In the preliminary stage of data reduction, the measured complex correlations were corrected for variations in receiver gains and local oscillator line lengths, then divided by the complex interferometer gains determined from the calibrator observations to obtain the (unnormalized) calibrated complex visibilities. These visibilities should be thought of as the fundamental output of the radio telescope, on which all subsequent analysis techniques operated.

4.2. MAPPING THE LINE INTEGRATED BRIGHTNESS

Let h_i and δ_i be the hour angle and declination, respectively, of the i^{th} integration. The spatial frequency domain coordinates (u_i, v_i) of the smallest-spacing interferometer for this integration are given by

$$u_i = B_x \cos h_i - B_y \sin h_i \qquad (1)$$

---

[3] Throughout this report, longitudes on Jupiter are based on System III, epoch 1967.0 (Carr 1971). Longitudes measured in this system agreed with those measured in the older System III, epoch 1957.0, on 1 January 1967 at 0^h UT, but the new system is based on a rotation period of $9^h\ 55^m\ 29.75^s$, which is 0.38^s longer than that used for System III (1957.0). The older value is now believed to be in error. The two systems are related by

$$\lambda_{III}(1967.0) = \lambda_{III}(1957.0) - 3.38222^o \text{ (epoch - 1967.0)}.$$

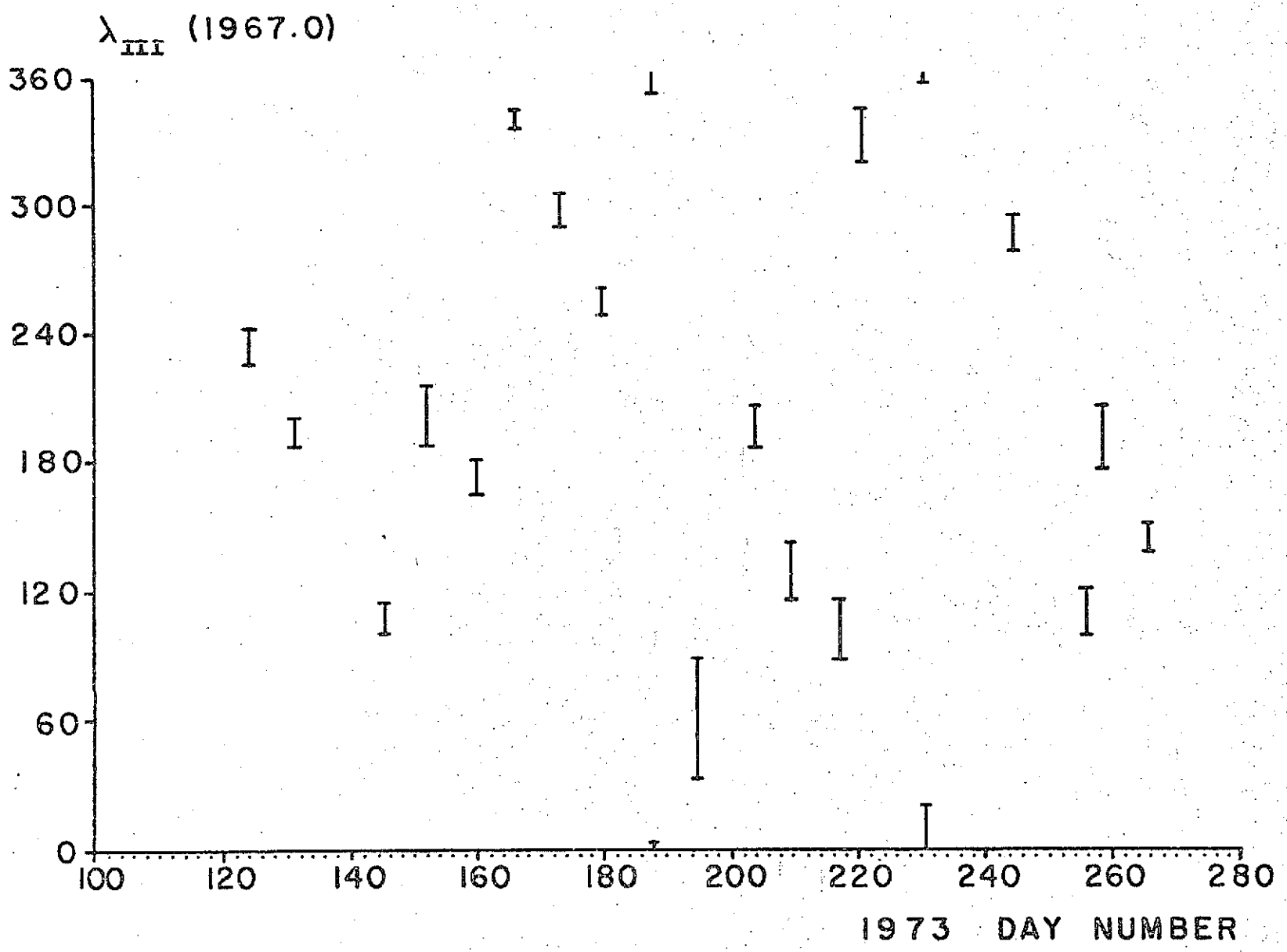

FIG. 2. Weekly observing program: dates of observations and Jovian central meridian longitudes.

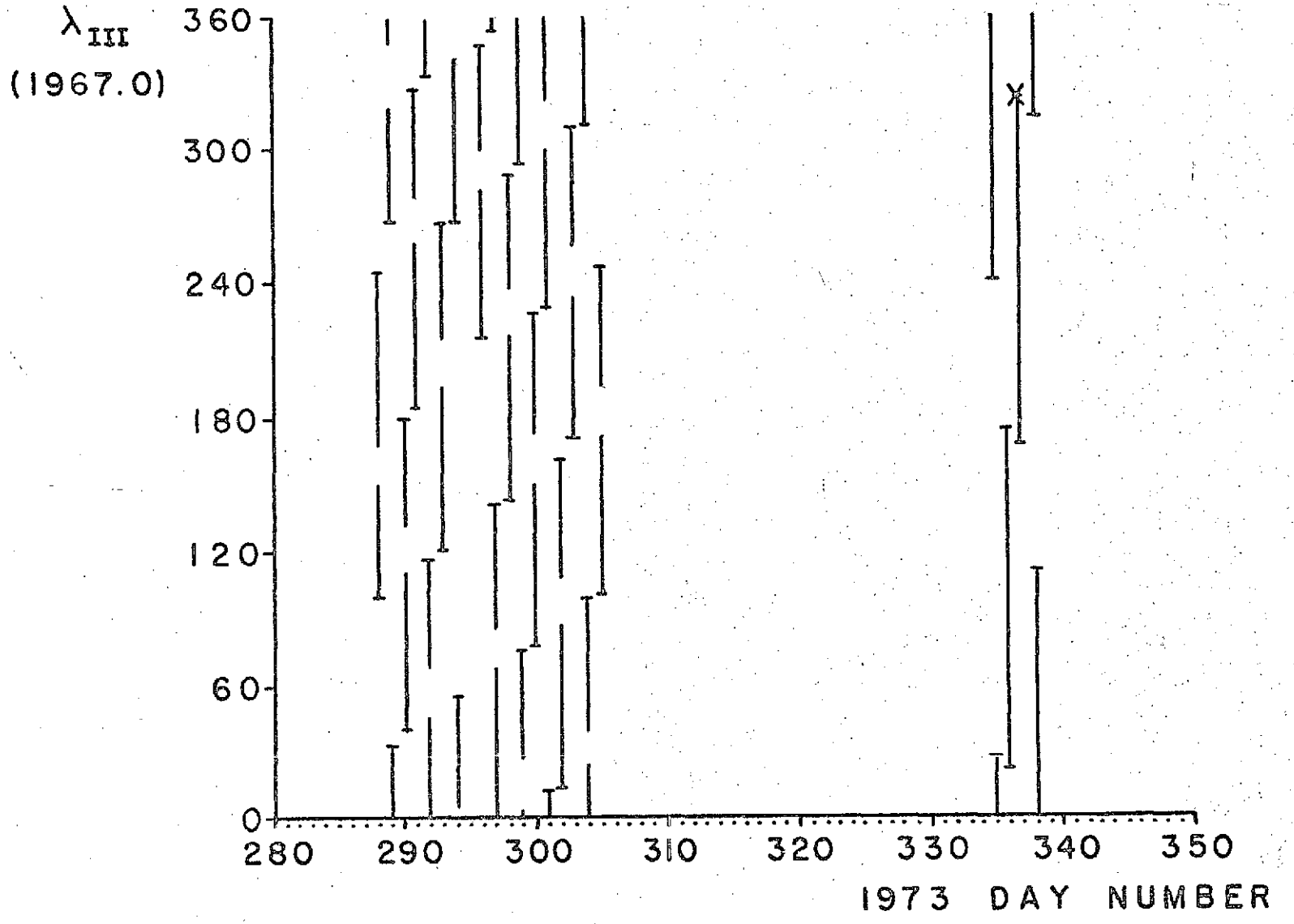

FIG. 3. Daily and flyby observing programs: dates of observations and Jovian central meridian longitudes. A cross marks the time of Pioneer 10 periapsis.

$$v_i = B_z \cos \delta_i - \sin \delta_i (B_x \sin h_i + B_y \cos h_i) \qquad (2)$$

where B_x, B_y, and B_z are components of the shortest baseline vector, measured in wavelengths in a rectangular coordinate system whose x-axis points to the west horizon and whose z-axis points to the north celestial pole. Then if we number the interferometers in order of increasing baseline length, the baseline vector of the k^{th} interferometer (known as Channel k) is very nearly k times the shortest baseline, so its spatial frequency is just (ku_i, kv_i).

Given measurements of the complex visibilities at N hour angles, we denote the i^{th} measurement on the k^{th} channel by $V_{i,k}$; this can be expressed in polar form as $A_{i,k} \exp(j\phi_{i,k})$ with $j = \sqrt{-1}$. From these measurements it is possible to estimate the two-dimensional brightness distribution of the source. Several methods exist for forming this estimate (D'Addario 1974). Here we use a direct Fourier transform of the measurements. Let $b(x,y)$ be the estimated brightness distribution as a function of rectangular coordinates on the sky. We take x to be the angular distance from the center of the field of view in hour angle and y to be the distance from the center in declination. The direct transform map is defined to be

$$b(x,y) = c\left\{F + 2 \sum_{i=1}^{N} \sum_{k=1}^{9} \alpha_{i,k} A_{i,k} \cdot \cos[2\pi k x u_i + 2\pi k y v_i + \phi_{i,k}]\right\}. \qquad (3)$$

The angular distances x and y are in radians, and the multiplier c determines the units of $b(x,y)$. F is the total flux density; since it is not directly measurable with multiplying interferometers, we estimate it to be equal to the magnitude of the smallest-spacing visibility. This is quite accurate for small-diameter sources, including Jupiter. The coefficients $\alpha_{i,k}$ are weights which can be adjusted to improve the side-lobe structure of the map at the expense of loss in resolution. If $\alpha_{i,k}$ is proportional to the integrating time of the i^{th} measurement, we say that equal-time weighting has been used; then if the noise power is the same on all channels, this results in a map with maximum signal-to-noise ratio. It is therefore the weighting which we use here.

Due to the single redundancy in the Stanford interferometer, two independent measurements of the smallest-spacing visibility are made. The visibility used in (3) for this spacing is the complex average of the two measurements.

As mentioned earlier, due to the limited rotation of the interferometer baseline with respect to Jupiter, resolution in the north-south direction is poor. The information contained in $b(x,y)$ is inherently one-dimensional. It is convenient to present the data by line integrating (3). Let $b_\theta(r)$ be the line integral of $b(\cdot,\cdot)$ as a function of distance in the direction θ. θ is called the scan position angle and is measured in degrees east of north on the sky. The line-integrated brightness is then

$$b_\theta(r) = \int\int b(x,y)\,\delta(x\cos\theta + y\sin\theta - r)\,dx\,dy\,, \qquad (4)$$

where $\delta(\cdot)$ is the Dirac delta function and the integration is performed over the field of view.

We define the position angle of an integration as that of the projection of the interferometer baselines on the sky.[4] While it is possible to evaluate (4) for any value of θ, high resolution scans are obtained only if we choose θ to be comparable to the position angles of the integrations used in computing the map by (3). Figures 4-6 contain representative line-integrated brightness plots from the weekly, daily and fly-by observations. The scan position angle and the range of integration position angles are noted on each plot. Also shown is the ideal point source response for the hour angle coverage obtained.

Figure 7 gives a similar line-integrated brightness plot using all of the data from the daily program. This "grand average" results from 57.5 hours of observation. It does not take into account the change in Jupiter's apparent size during the 18 days, but this amounted to only 6 per cent.

4.3. PARAMETERS OF THE BEST-FIT UNIFORM DISK

It is apparent from figures 4-6 that most of the radiation is due to the thermal emission from the disk. At our resolution, a reasonable model for the thermal source is a uniform temperature disk. A circular disk is characterized by a temperature T, an angular semidiameter r, and center position (x_0, y_0), and has a visibility function given by

[4] Such a concept is useful only when all the baselines are collinear, as they are for the Stanford array, and only when the integrating time is short.

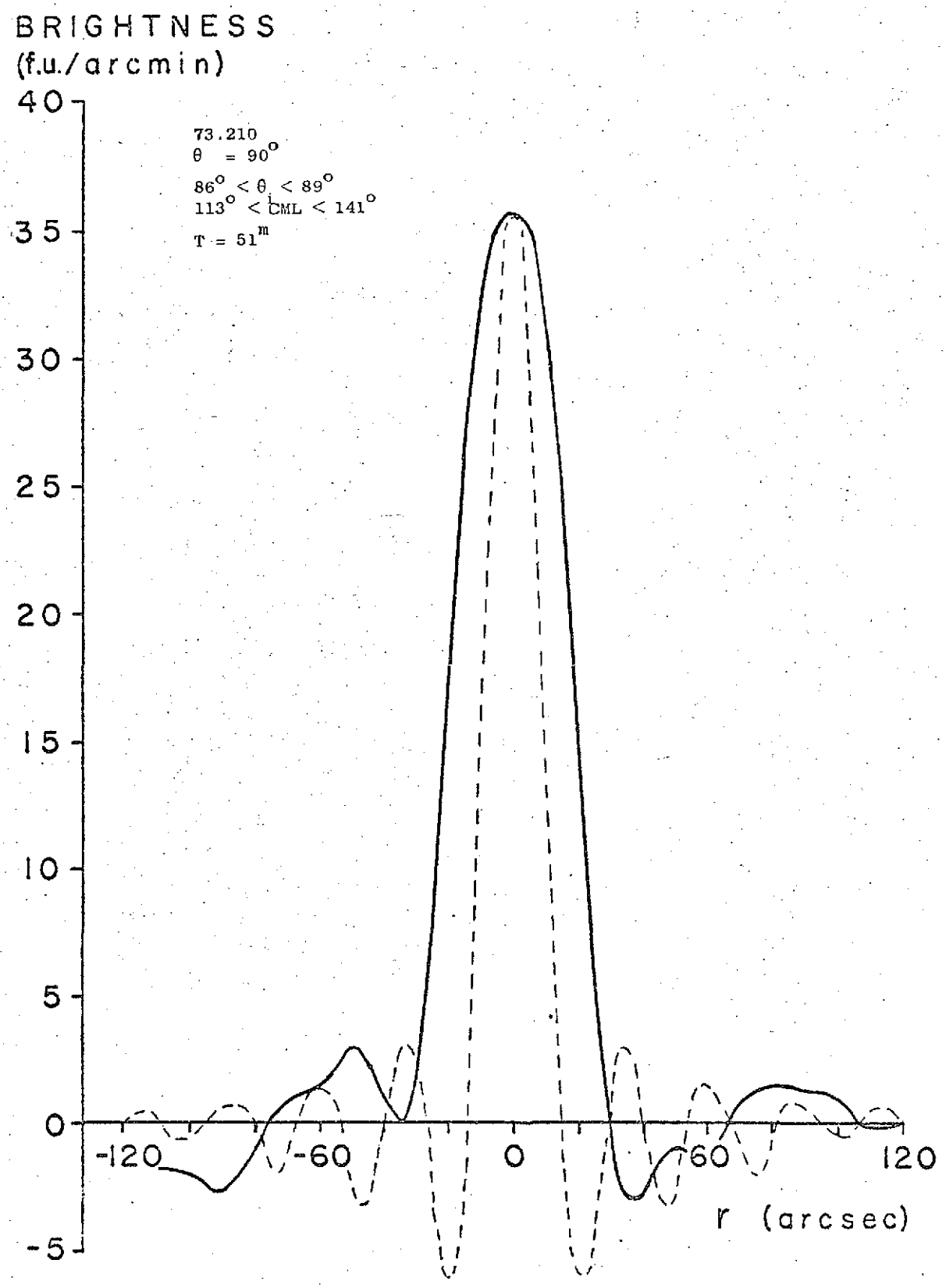

FIG. 4. Solid curve: estimated line-integrated brightness on 29 July 1973 (weekly program). Dashed curve: response to a point source (arbitrary ordinate scale). East is on left. θ is the scan position angle, θ_i is the integration position angle, and T is the total observing time.

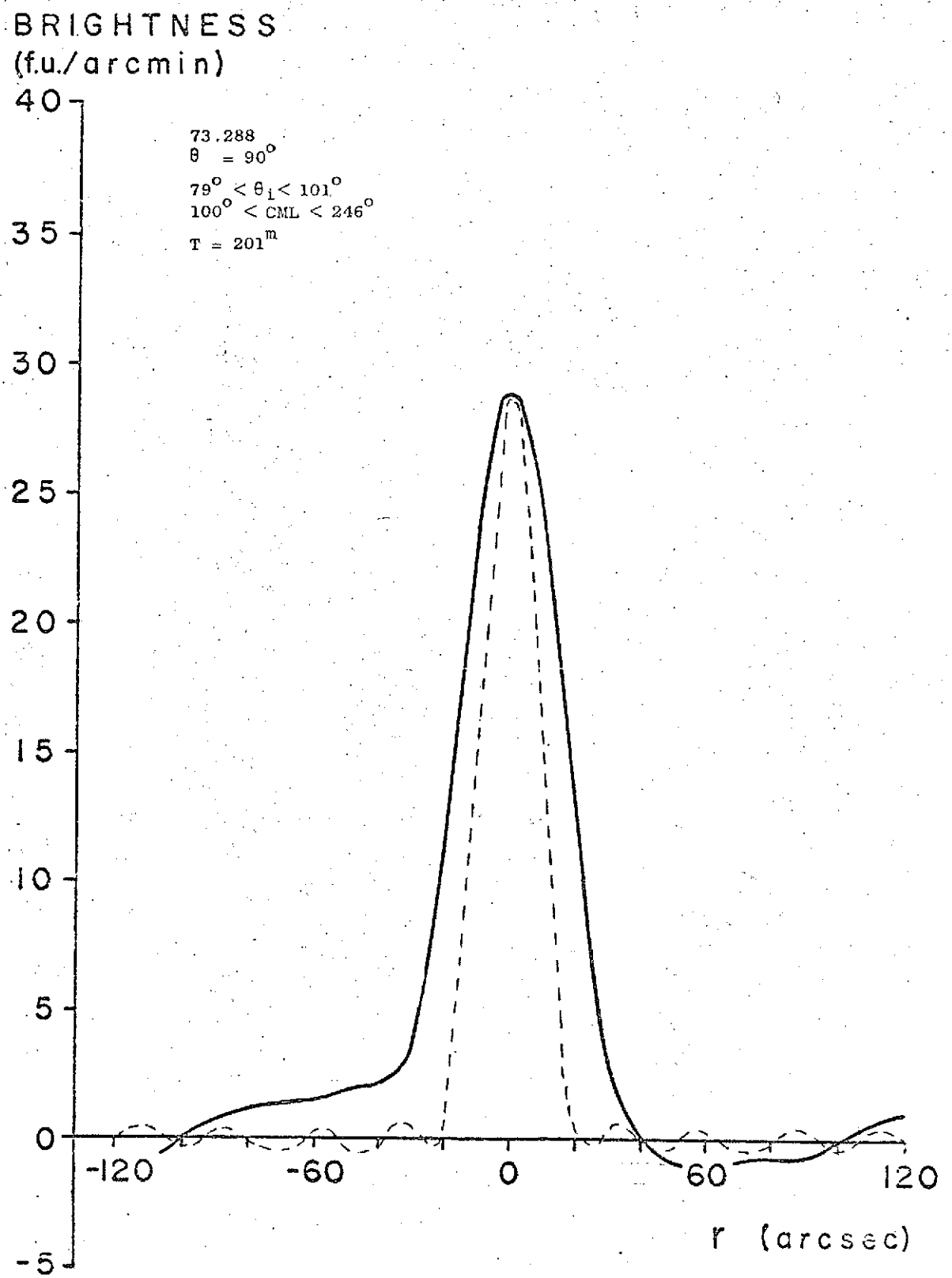

FIG. 5. Estimated line integrated brightness on 15 October 1973 (daily program). Dashed curve: response to a point source (arbitrary ordinate scale). East is on the left. θ is the scan position angle, θ_i is the integration position angle, and T is the total observing time.

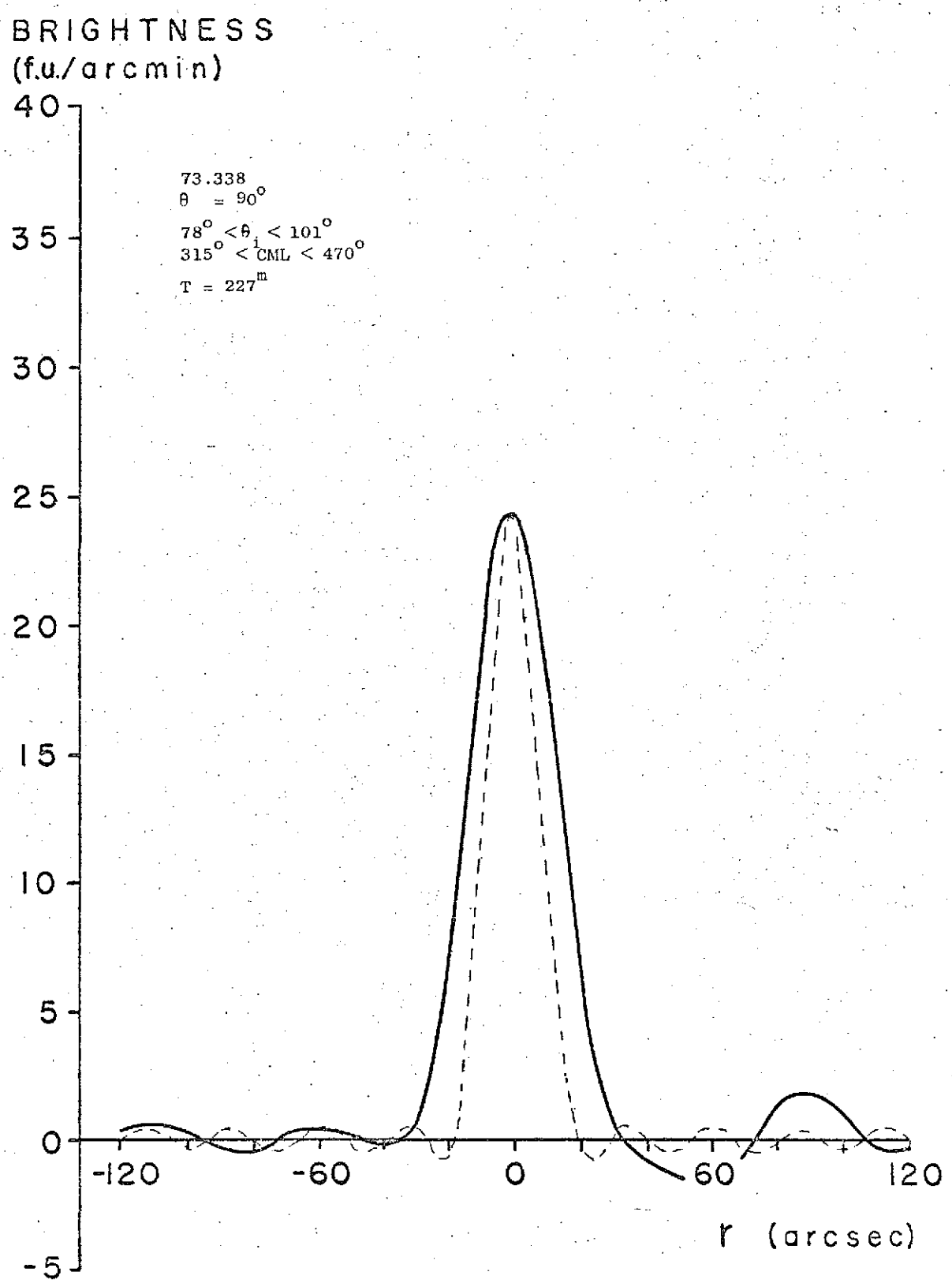

FIG. 6. Estimated line integrated brightness on 5 December 1973 (flyby program). Dashed curve: response to a point source (arbitrary ordinate scale). East is on the left. θ is the scan position angle, θ_i is the integration position angle, and T is the total observing time.

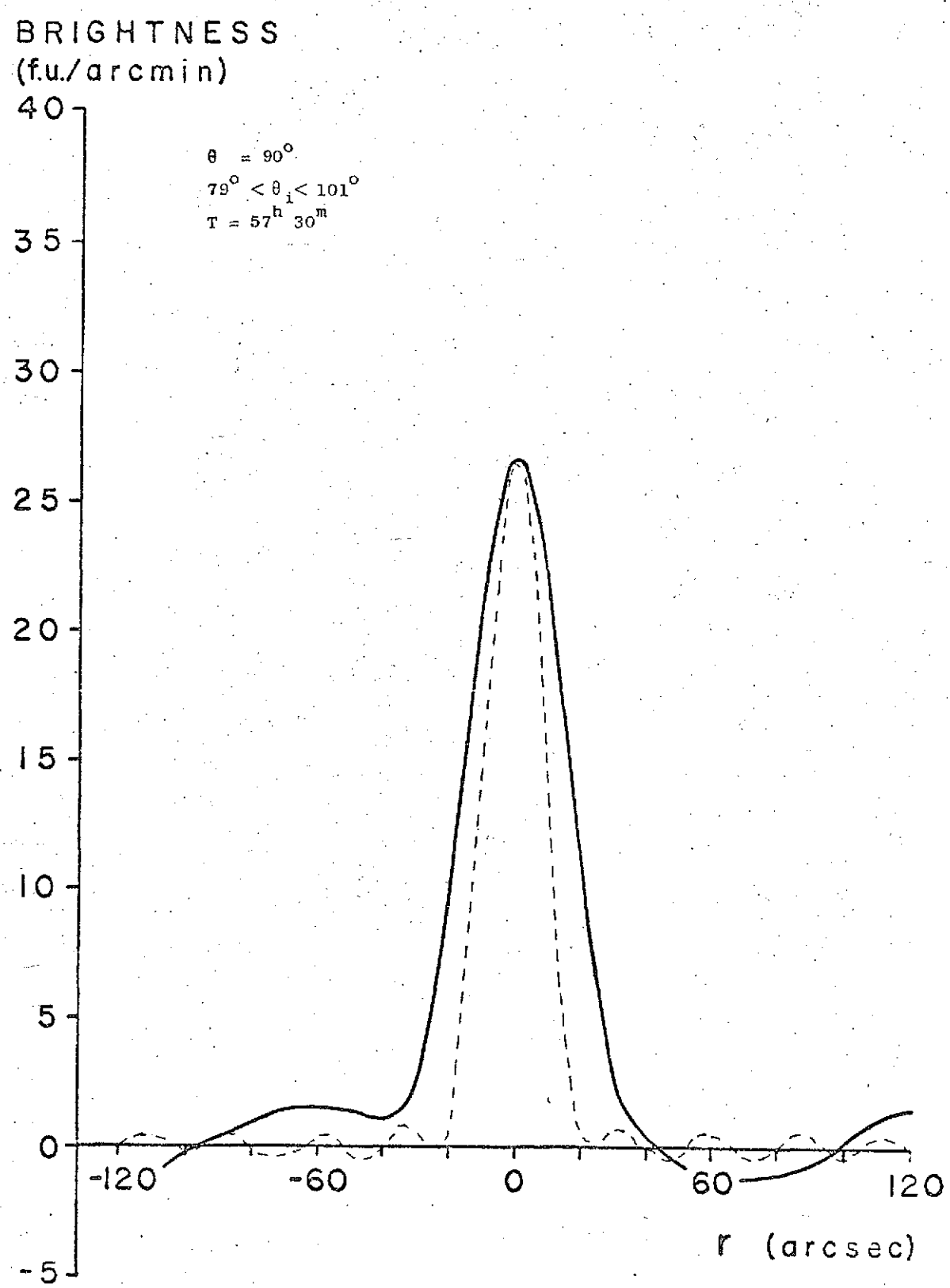

FIG. 7. Estimated line integrated brightness calculated from all observations in the daily program (17 days). Dashed curve: response to point source (arbitrary ordinate scale). East is on the left. θ is the scan position angle, θ_i is the integration position angle, and T is the total observing time.

$$V(u,v) = \frac{2kT\pi r^2}{\lambda^2} \quad \frac{J_1(2\pi r\sqrt{u^2+v^2})}{\pi r\sqrt{u^2+v^2}} \exp[j2\pi(x_0 u + y_0 v)] \qquad (5)$$

where $J_1(\cdot)$ is the first order Bessel function of the first kind.

The oblateness of the Jovian disk and the non-zero position angle of the rotation axis produce additional complications. The former causes a change of scale and the latter causes a rotation of coordinates. Taking these into account, (5) becomes

$$V(u,v) = \frac{2kT\pi r_e r_p}{\lambda^2} \quad \frac{J_1(2\pi Rq)}{\pi Rq} e^{j2\pi Xq} \qquad (6)$$

where

$$q = \sqrt{(u^2 + v^2)} ,$$

$$R = \sqrt{r_e^2 \sin^2(\theta_i - \theta_p) + r_p^2 \cos^2(\theta_i - \theta_p)} ,$$

$$X = x_0 \sin(\theta_i - \theta_p) + y_0 \cos(\theta_i - \theta_p) ,$$

$$\theta_i = 90^o - \tan^{-1}(v/u),$$

r_e and r_p are the equatorial and polar semidiameters, respectively, and

θ_p is the position angle of the rotation axis (measured east of north on the sky).

The measured visibilities can now be used to determine the disk parameters in (6). With our linear array and 5^m integrating time, each integration results in visibilities at 9 values of q and one value of the integration position angle θ_i. Fitting (6) to the data from a single integration then allows us to determine three parameters, namely R, X, and $F = 2kT\pi r_e r_p/\lambda^2$, where F is the total flux density. Actually, we computed the least-squares values of these parameters using 25^m averages of the measurements, during which θ_i varied by no more than 2^o. The results for the weekly and daily observing programs are shown in Figs. 8 and 9, respectively. For the range of θ, θ_p, r_p, and r_e encountered in these observations, $1.058r_p \leq R \leq 1.068r_p$ (assuming 7% oblateness so that $r_e = 1.07r_p$); thus 1.063 times the polar semidiameter of the optical disk is plotted for comparison with the fitted values of R. The brightness temperature plotted in the figures is that of a uniformly bright ellipse producing the fitted flux density F and having semi-minor axis equal to the optical polar semidiameter and having 7% oblateness.

The scatter in the position parameter X shows that the centroid of the radio emission is always within about $2''$ of the center of the optical disk, as expected.

The close agreement between the computed best-fit disk radius and the optical radius indicates an absence of any conspicuous limb brightening or darkening.

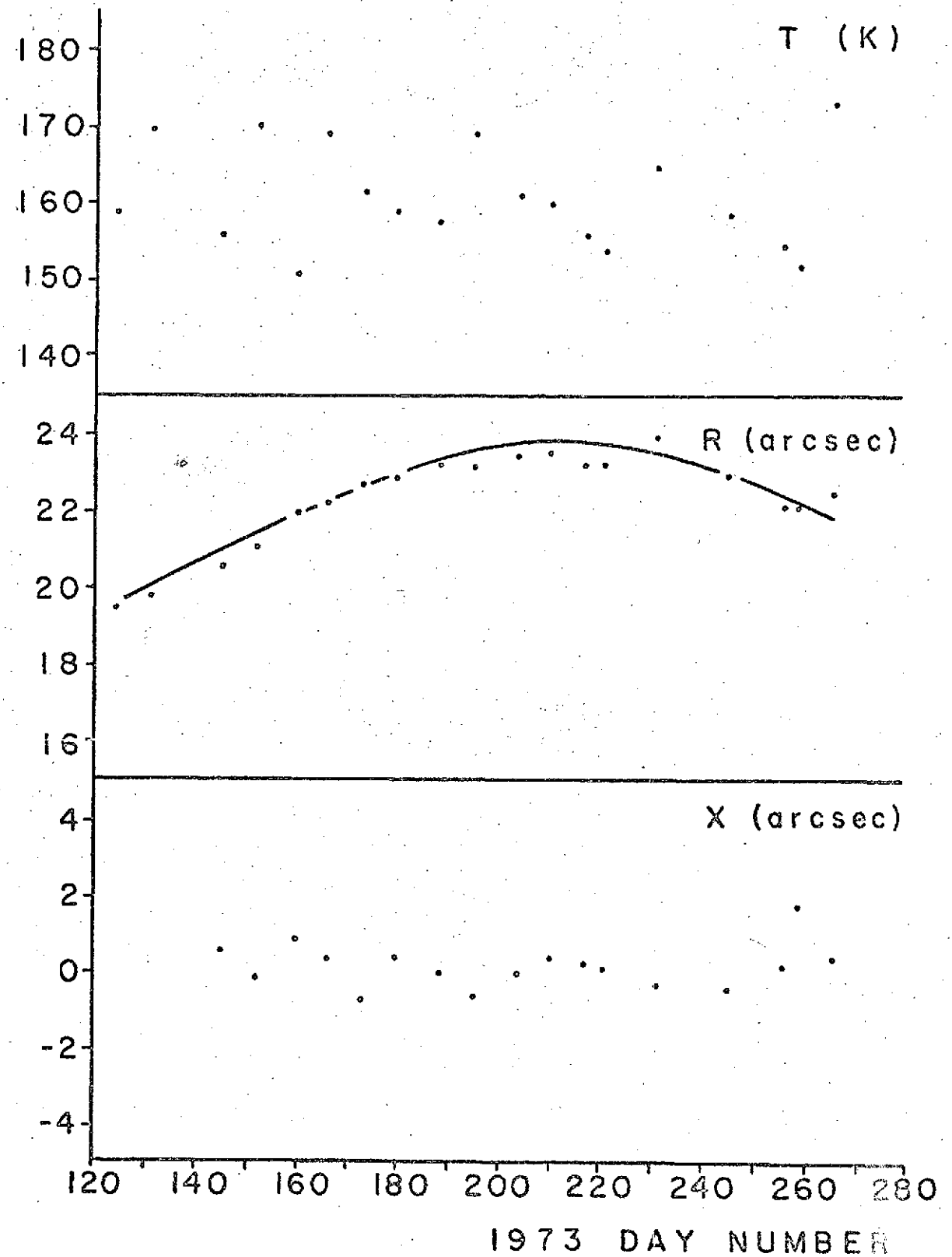

FIG. 8. Parameters of the best fit uniform-brightness disk for the weekly observations. T is brightness temperature, R is the radius, and X is the distance from the center of the optical disk. The solid curve is 1.063 r_p, where r_p is the polar semi-diameter of the optical disk.

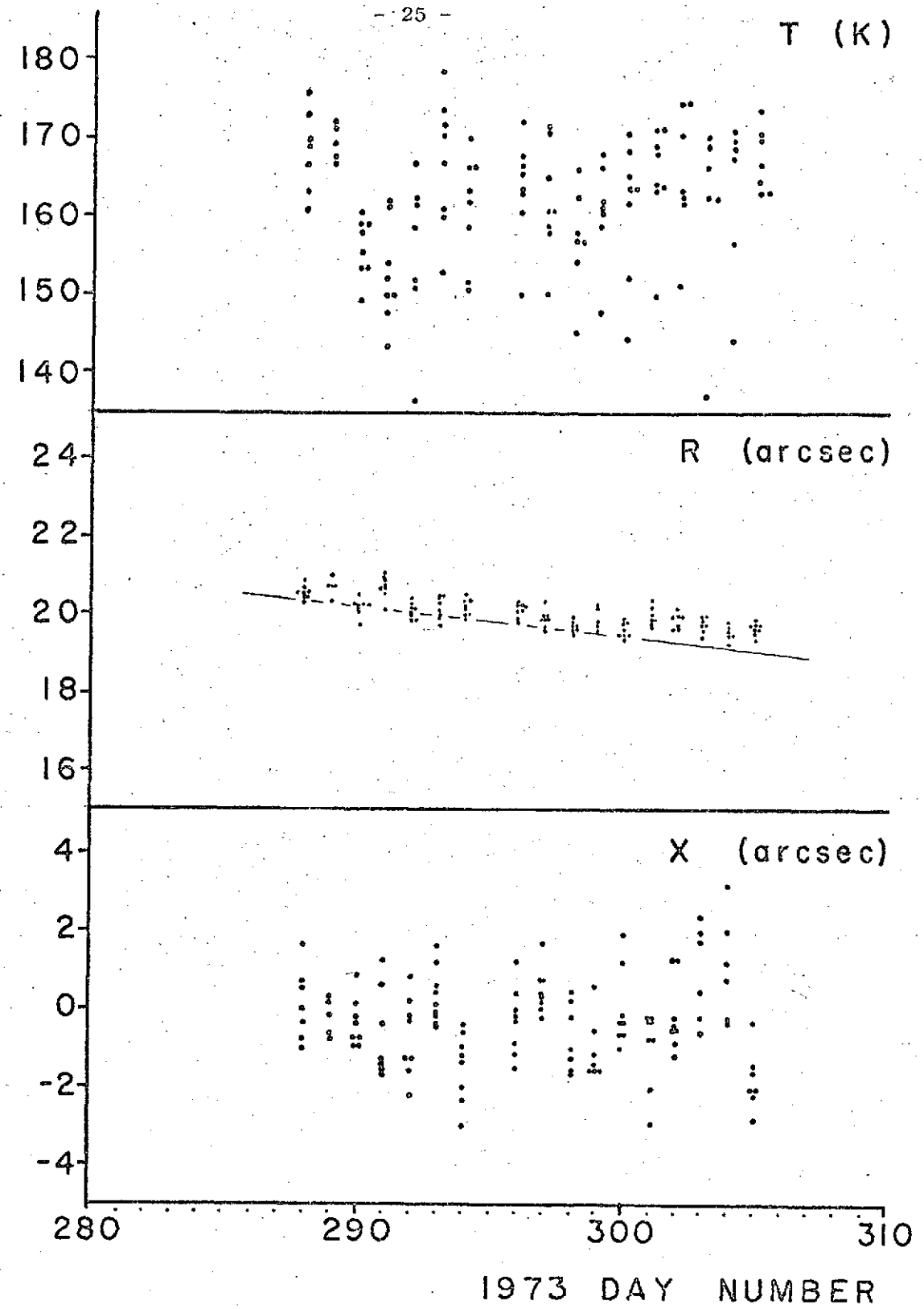

FIG. 9. Parameters of the best fit uniform-brightness disk for each 25^m average from the daily observations. Notation same as Fig. 8.

The temperatures show considerable scatter, but their mean value of about 160 K is in good agreement with single-antenna measurements made above and below 2.8 cm (Dickel et al. 1966). To see whether the scatter can be attributed to variations with Jovian CML, we constructed the plot of Fig. 10, using the daily data. No correlation with CML is apparent.

4.4. RESIDUAL VISIBILITIES AFTER SUBTRACTION OF THE BEST-FIT DISK

If we suppose that the observed radiation from Jupiter consists of a disk-like component, primarily of thermal origin, and a non-disk component, primarily non-thermal, then subtraction of the visibilities due to the best fit disk (computed from equation (6)) from the observed visibilities should yield a residual equal to the visibilities due to the non-disk component alone. This might be expected to allow study of the non-thermal radiation from Jupiter's magnetosphere. However, it should be kept in mind that such a separation of the two components is particularly sensitive to measurement errors because each residual visibility is the difference between two large numbers which are approximately equal (i.e., most of the radiation is in the disk-like component).

Shown in Figure 11 is a plot of the estimated line integrated brightness for 25^m of data from the daily observations, along with the corresponding line integrated brightness computed from the residual visibilities after disk subtraction. Note that the residuals are plotted with an expanded ordinate scale. The residual visibilities from all such 25^m averages taken on each day of observations were then used to compute daily plots of the residual brightness; representative results are given in Figure 12.

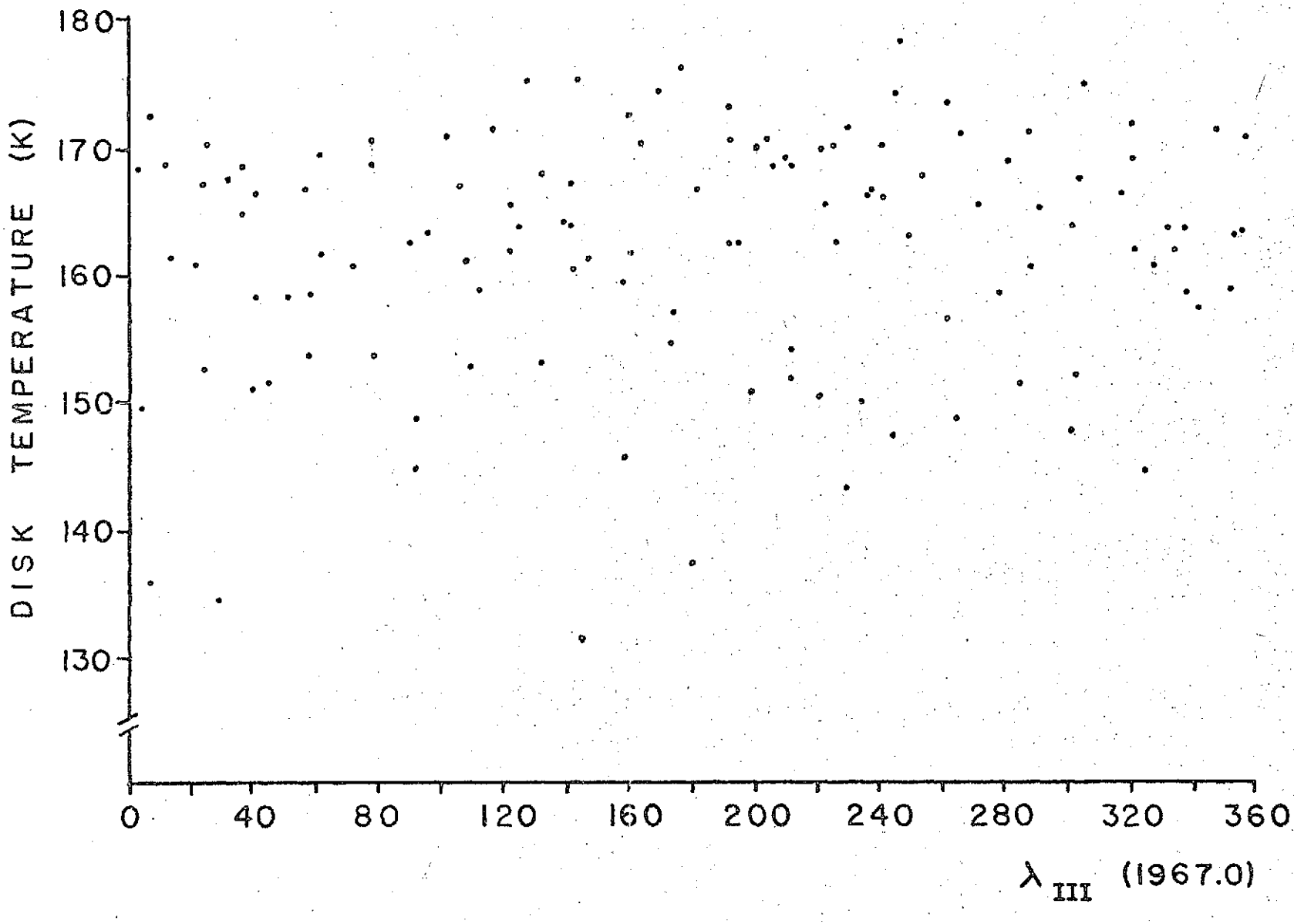

FIG. 10. Brightness temperature data from Fig. 8 (based on 25^m averages from the daily program), plotted as a function of Jovian central meridian longitude.

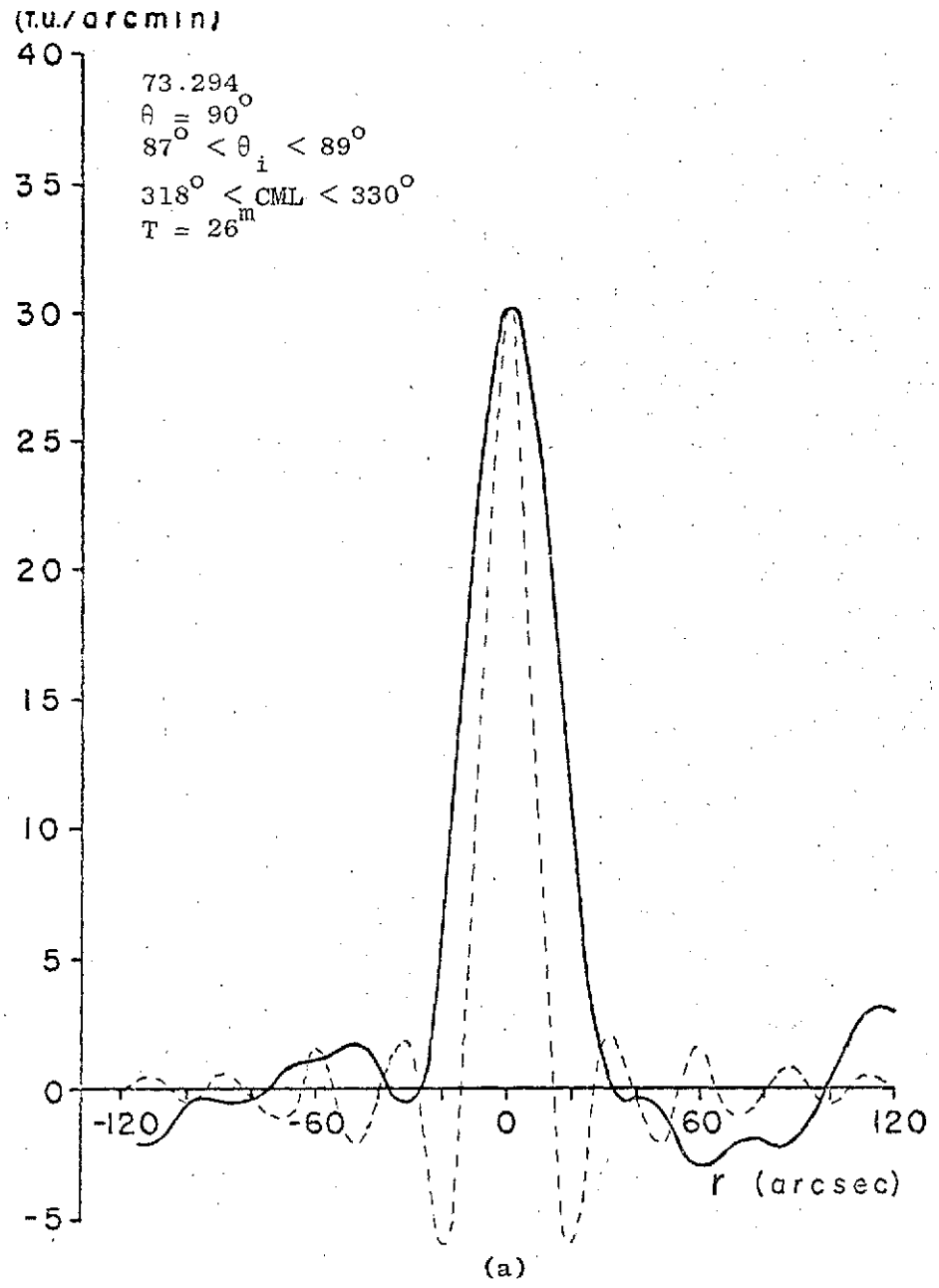

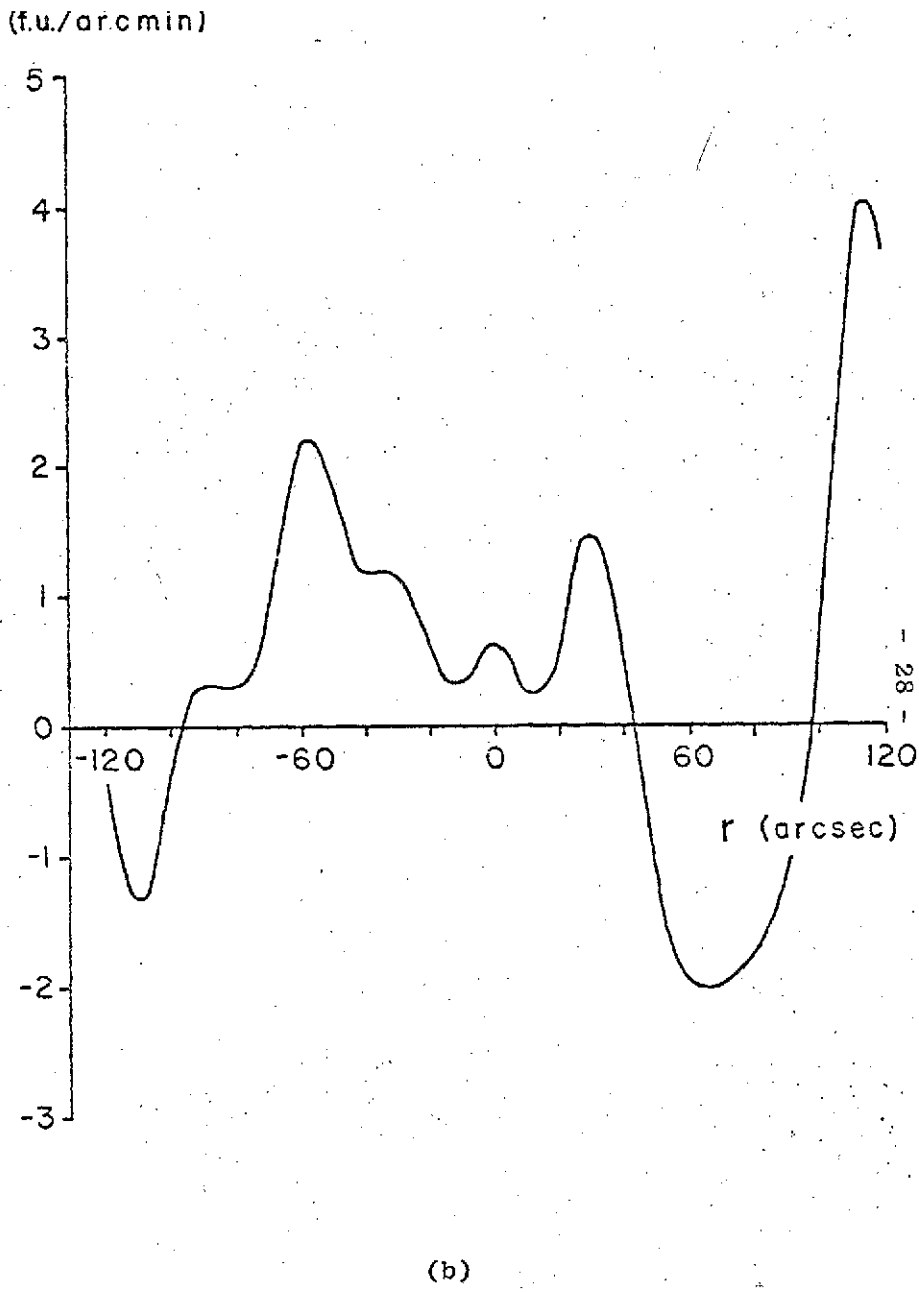

FIG. 11. (a) Estimated line integrated brightness on 21 October 1973, computed from 25^m of data. (b) Estimated line integrated brightness computed from the residual visibilities obtained by subtracting the best-fit disk from the data used to compute (a).

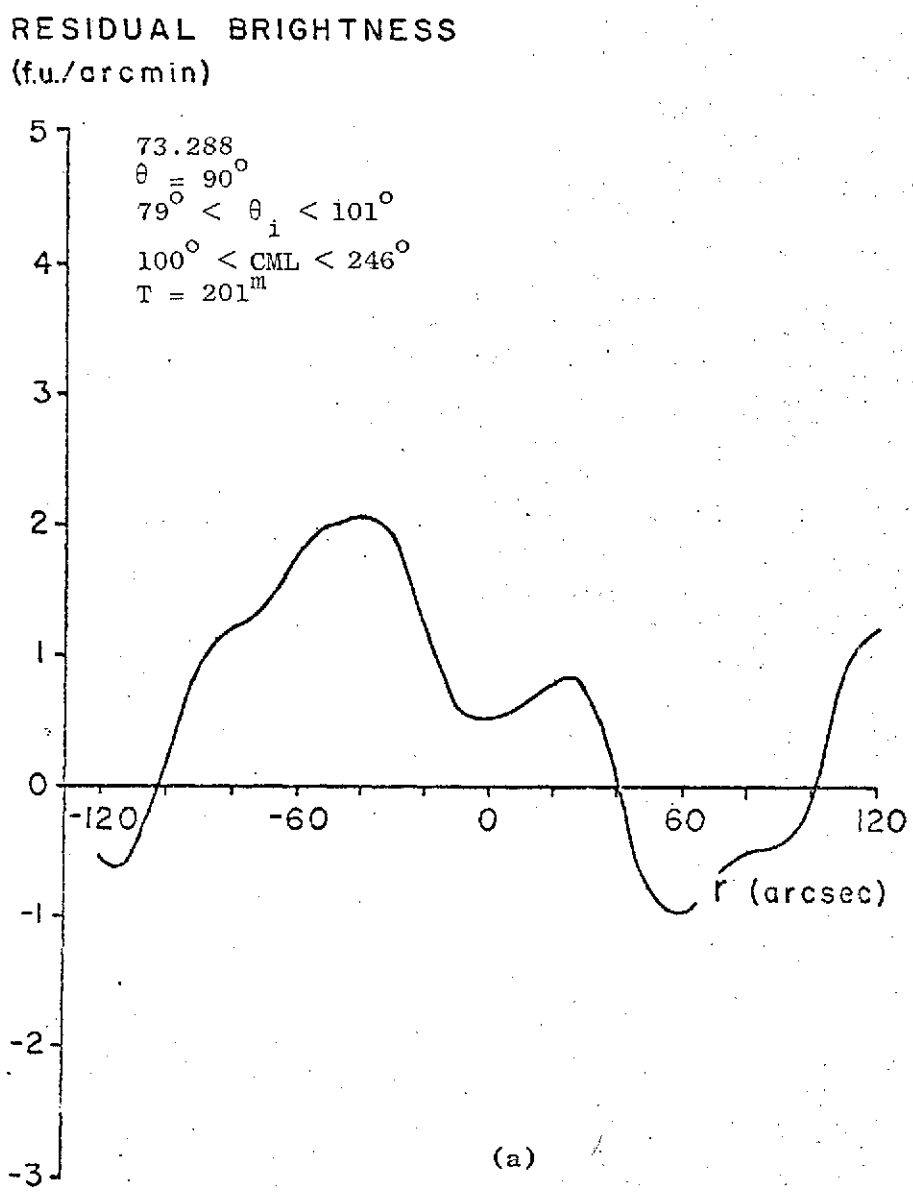

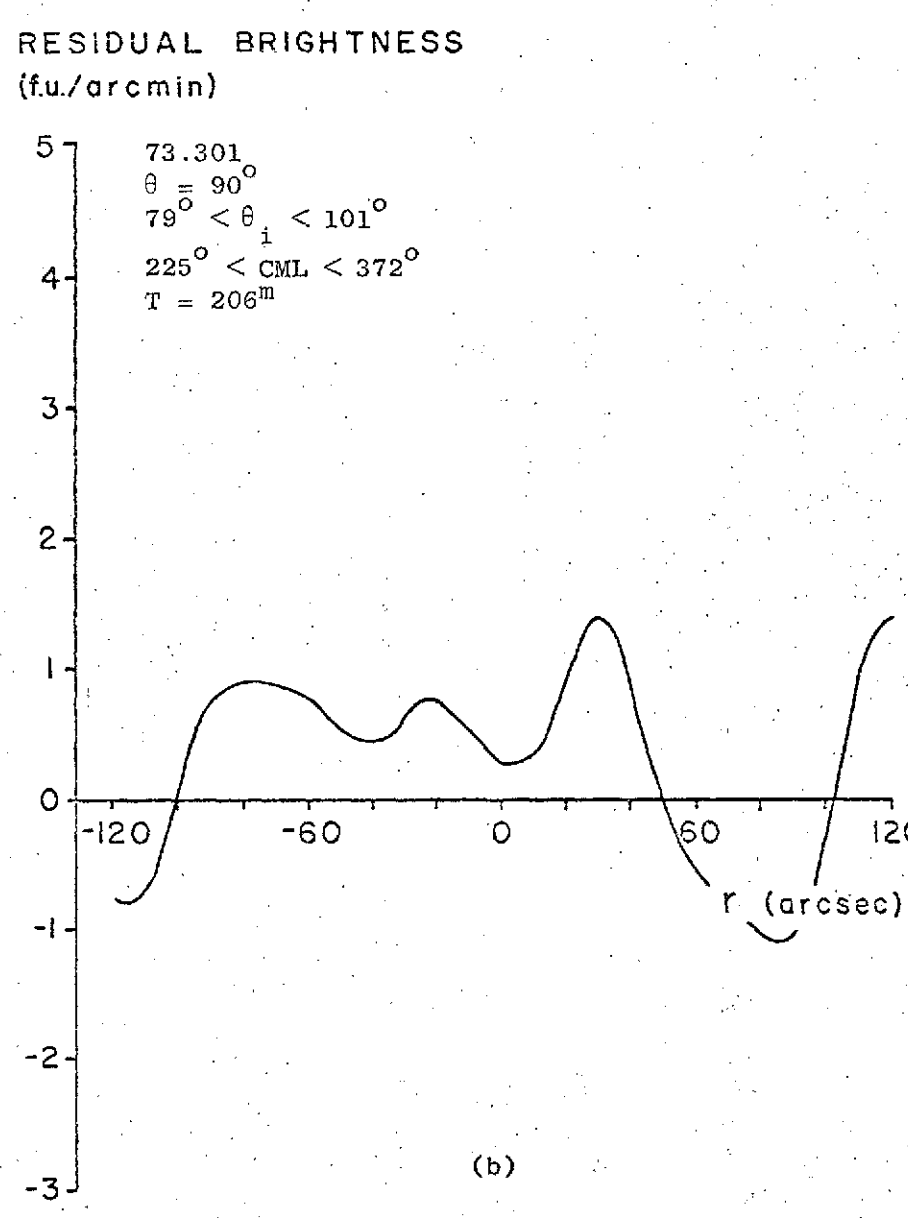

FIG. 12. Residual brightness computed from all 25m residuals on a given day. (a) 15 October 1973. (b) 29 October 1973.

The residual brightness may be thought of as consisting of two additive components: (1) our response to the non-disklike component of radiation from the vicinity of Jupiter, and (2) the difference between our actual response to the disklike component and the "ideal" response, the latter having been subtracted from the measurements. In order to decide whether plots such as Figures 11b and 12 contain significant information about the non-disk component (1), we now examine the magnitude of the error component (2).

We prefer to work in the visibility domain, where the measurements were made. The errors include, first, random noise due primarily to the non-zero system temperature and receiver gain fluctuations; and second, systematic calibration errors. The former are well understood and can generally be reduced by averaging a longer series of similar observations. For most of our analysis, we used 25^m averages of the data, for which the r.m.s. complex noise[5] was $\sigma \approx 1.0$ f.u. in each interferometer channel.

Calibration errors, on the other hand, depend upon the source being observed. In general,

$$\epsilon_{i,k} \triangleq \hat{V}_{i,k} - V_{i,k} = V_{i,k}\left(\frac{g_{i,k}}{\hat{g}_{i,k}} - 1\right)$$

where $\epsilon_{i,k}$ is the error in visibility for the i^{th} integration on the k^{th} interferometer; $\hat{V}_{i,k}$ and $V_{i,k}$ are the measured and true visibilities, respectively; and $\hat{g}_{i,k}$ and $g_{i,k}$ are the assumed and true complex gains. Our investigations show that errors up to 15% can be expected: i.e., $|\epsilon| \lesssim 0.15|V|$. Furthermore, the amplitudes of the $g_{i,k}$ are known somewhat better than their phases. From the pointing residuals and from studies of the antenna gains vs. zenith angle, we expect amplitude errors of 5 to 8%.

[5] We define the r.m.s. of a complex random variable x as $(E\,|x - Ex|^2)^{\frac{1}{2}}$ where E denotes the expectation operator.

From the full-sky phase residuals, we expect phase errors at Jupiter's declination of ~.02 cycle, which corresponds to a 13% gain error. Some of the phase errors were removed, however, by applying phase corrections derived from observations of PKS 0834-20, which is very near Jupiter's declination. We therefore believe that 15% ($=\sqrt{.08^2 + .13^2}$) is a conservative upper bound to the uncorrected calibration error in each interferometer.

Table 2 summarizes these results for a uniform disk at 160 K with radius 20″ observed for 25^m at meridian crossing. The disk visibilities $|V_k|$ were calculated using equation (5), and a "detection limit" for each channel is taken to be three times the r.m.s. noise plus $0.15|V_k|$. Residuals larger than the detection limit may be taken to be due to non-disk radiation from Jupiter. Columns (5) and (7) of Table 2 give the observational results: for the daily program, the amplitudes of the residuals obtained on each day from the 25^m of data taken nearest meridian crossing were averaged channel by channel over the 17 days. For the weekly program, a similar average over 5 weeks was computed, using the weeks for which the optical radius of Jupiter was 20″ ±1″.

It should be apparent from the table that no non-disk radiation can be considered detected. From this fact, we can at least derive an upper limit to the non-disk flux density at 10 GHz. If this component arises from a broad radiation belt, so that much of the emission occurs across the face of the disk as well as off to the sides, then it cannot be well separated from the disk component by the large-spacing interferometers; in this case, we can say only that it must be less than about 3 f.u. On the other hand, if the non-disk component arises from a narrow belt at $1.8R_J$, then from the lack of detection on channels 5, 6, and 7 we can place an upper limit of about 2 f.u. on the non-disk flux.

Table 2

LIMITS TO THE NON-DISK FLUX

(1) Interferometer Channel k	(2) Spatial Frequency	(3) $\lvert V_k \rvert$ for a 160 K, 20″ radius uniform disk	(4) Daily Observations: Detection Limit*	(5) Daily Observations: Residual Amplitude†	(6) Weekly Observations: Detection Limit*	(7) Weekly Observations: Residual Amplitude‡
1	$(252'')^{-1}$	16.1 f.u.	3.1 f.u.	1.5 f.u.	3.8 f.u.	1.6 f.u.
2	$(126'')^{-1}$	14.7	2.9	1.8	3.5	2.1
3	$(84'')^{-1}$	12.4	2.6	2.4	3.2	1.6
4	$(63'')^{-1}$	9.6	2.2	1.6	2.8	2.2
5	$(50'')^{-1}$	6.72	1.7	0.7	2.3	0.8
6	$(42'')^{-1}$	3.88	1.3	1.1	1.9	0.5
7	$(36'')^{-1}$	1.41	0.9	0.5	1.6	0.5
8	$(32'')^{-1}$	0.46	0.8	0.4	1.4	0.4
9	$(28'')^{-1}$	1.67	1.0	0.6	1.6	0.3

*Detection limit = $3\sigma + 0.15\lvert V_k \rvert$, where $\sigma = 1.0$ f.u./$\sqrt{\text{number of days}}$

†Mean over 17 days, 25^m per day

‡Mean over 5 days, 25^m per day

We also sorted the 25^m residual visibilities by Jovian CML and examined the maps resulting from each 24^o of CML, but no systematic trends could be found.

Finally, in Figure 13 we give the estimated line-integrated brightness computed from the 25^m residuals of all of the data taken in the daily program. This might be compared with Figure 7, which gives the tot brightness using the same data. Examining Figures 11-13 and similar plot made from different subsets of the observations, we note a consistent feature at +30″, which is about 1.5 R_J to the west of Jupiter. It contains about 0.2 f.u., and because of its consistent appearance it seems likely to be actually associated with Jupiter. On the other hand, the region of large negative "brightness" further to the west and the broad apparent emission to the east of Jupiter are probably due to measurement errors. Consequently, we do not consider these maps satisfactory and we do not think it possible to draw from them any conclusions about asymmetries in the non-disk brightness.

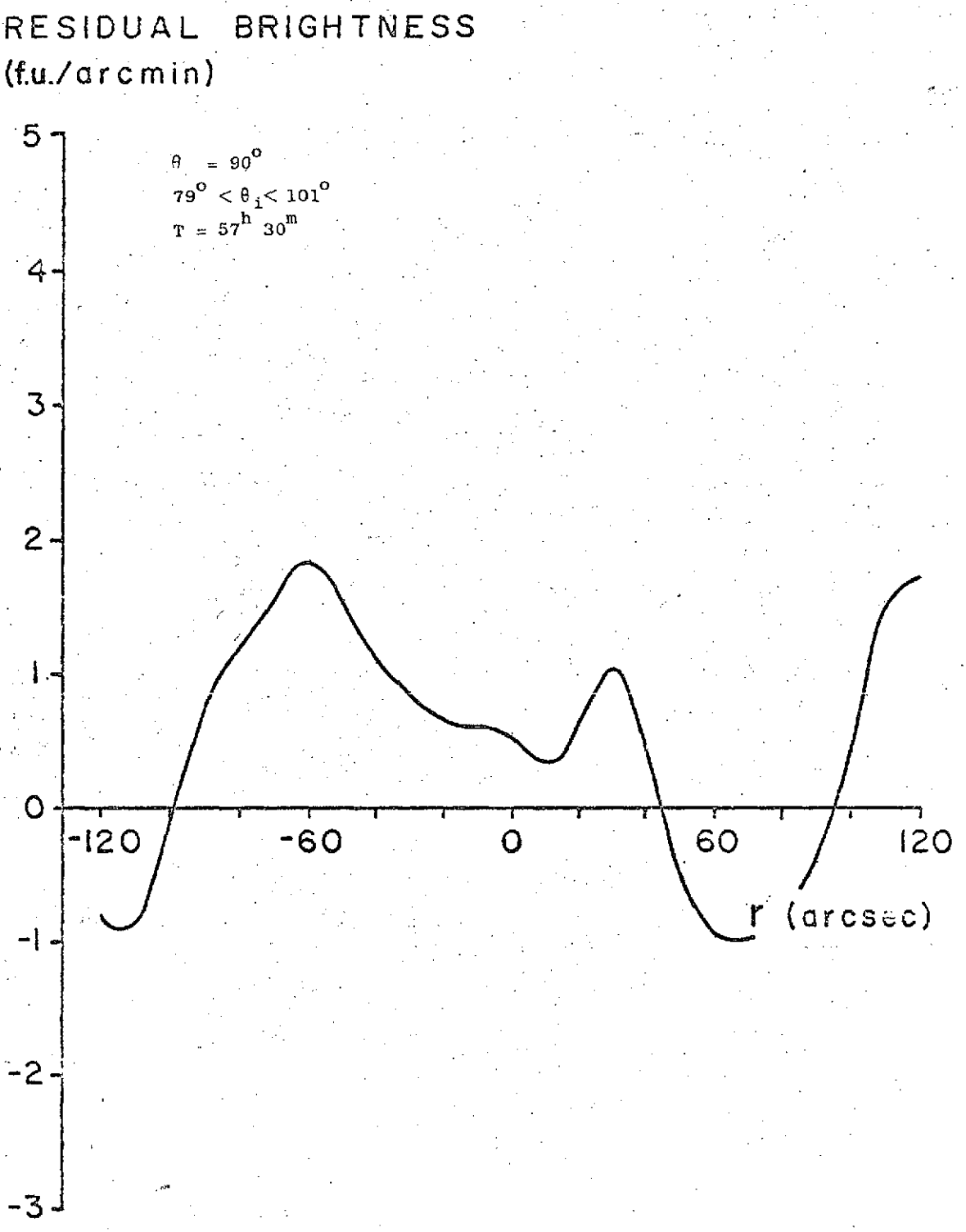

FIG. 13. Residual brightness computed from all 25^m residuals in the daily program (17 days of observations).

4.5. THE LINEARLY POLARIZED COMPONENT

An alternative approach to separating the thermal and non-thermal components is to make use of the strong linear polarization of the latter. With linearly-polarized feeds at fixed position angles, we expect to observe a variation in flux density with Jovian central meridian longitude of the form

$$F_{obs} = F_0 + 2F_1 \sin^2[\theta_r - \theta_p + \alpha \sin(\lambda-\lambda_0)] \qquad (7)$$

where F_0 and F_1 are the unpolarized and linearly polarized flux densities, respectively; θ_r and θ_p are the position angles of the receiving horns (E-vector) and of Jupiter's rotation axis (measured east of north on the sky); and $90^\circ - \alpha$ and λ_0 are the Jovian latitude and longitude, respectively, of the northern-hemisphere magnetic pole. This equation is based on modeling the polarized component as having constant total flux and a position angle always normal to Jupiter's magnetic dipole moment. It does not include the effects of beaming of the radiation in the magnetic equatorial plane (e.g. Gulkis and Gary 1971), which enhances the variation of F_{obs} with λ. In principle, to the extent that equation (7) is correct, one can determine F_0, F_1, α, and λ_0 from observations of F_{obs} vs. λ.

In our case, $\theta_r \equiv 0$ and $\theta_p = 344^\circ \pm 1^\circ$ throughout the period of observations in 1973. Using the Pioneer 10 results (Smith et al. 1974) that $\alpha = 15^\circ$ and $\lambda_0 = 196^\circ$ (System III, 1967.0), equation (7) results in the curve given in Figure 14. In comparing the present observations with these results, it was felt that a 4-parameter fit of (7) to the data was not justified in view of the measurement errors. Instead, the data were fitted to the simpler function

$$F_{obs} = F_0 + A \cos(\lambda-\lambda_0') \qquad (8)$$

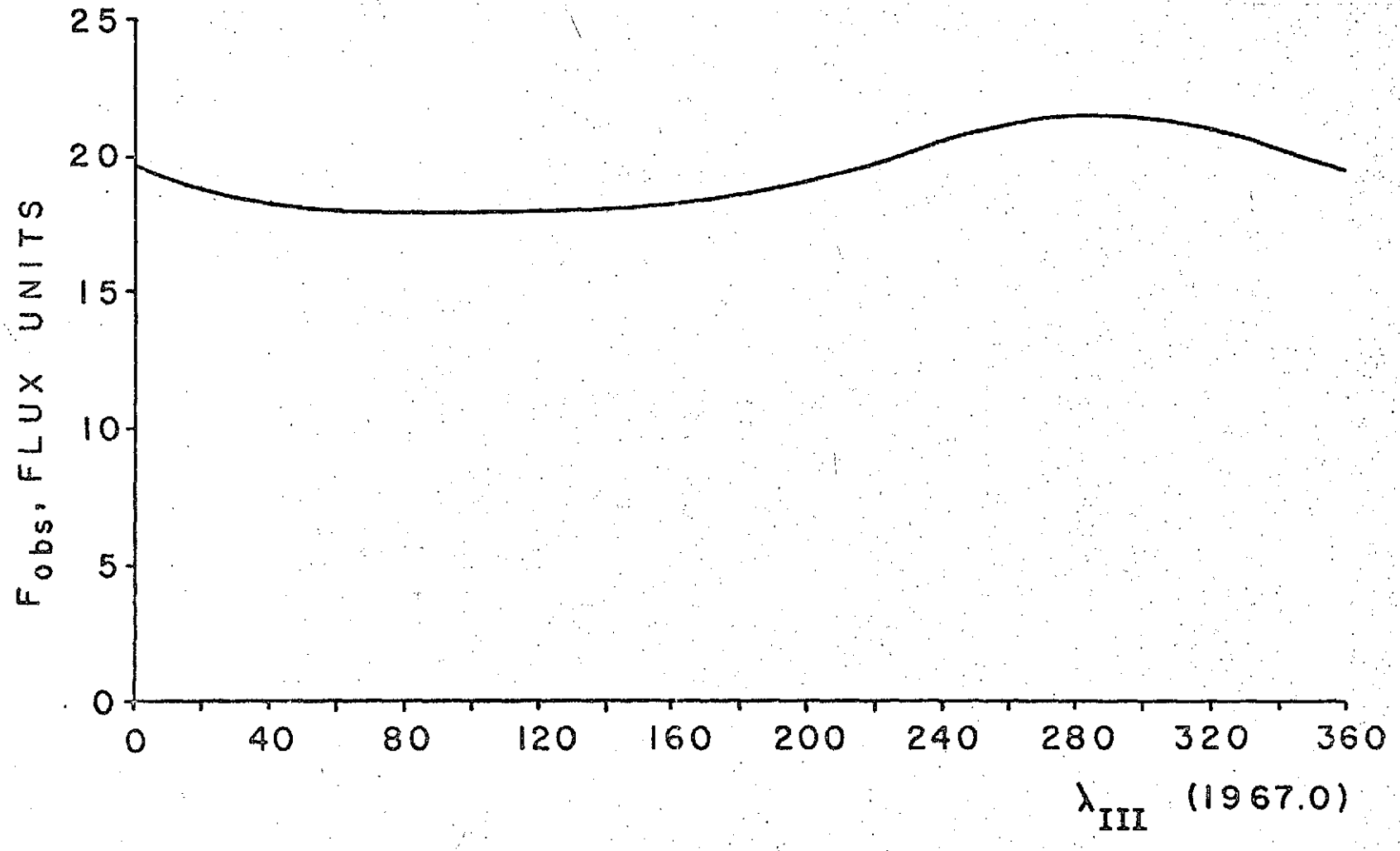

FIG. 14. Expected variation of observed flux density with CML due to rotation of the direction of linear polarization with respect to fixed, linearly polarized antennas. Based on the model of equation (7) with $F_0 = 18$ f.u., $F_1 = 6.7$ f.u., $\theta_r = 0$, $\theta_p = 344^\circ$, $\alpha = 15^\circ$ and $\lambda_0 = 196^\circ$.

which closely approximates (7) for our values of θ_r and θ_p, and for all reasonable values of α and λ_0. We also tried including second-harmonic terms in the fit, but the resulting coefficients were never significant. Comparing equations (7) and (8) gives

$$A \approx F_1[\sin^2(\theta_p-\alpha) - \sin^2(\theta_p+\alpha)] \qquad (9)$$

$$\lambda_0' \approx \lambda_0 + 90^\circ .$$

When the observations are made with an interferometer, we can interpret F_0 and F_1 in equations (7)-(9) as the unpolarized and linearly polarized parts of the complex visibility; that is, of the spatial frequency component corresponding to the interferometer's baseline. On our shortest baselines (spatial frequency $(252'')^{-1}$ at the meridian), Jupiter is essentially unresolved so that F_0 and F_1 are nearly equal to the total unpolarized and polarized fluxes. On the longer baselines, each part of the radiation can be expected to be partially resolved; but because the polarized and unpolarized parts have different spatial distributions, their ratio may be expected to depend on spatial frequency.

With this motivation, we used the daily series of observations to obtain values of F_0, A, and λ_0' for each of the 10 interferometers by a least squares fit to equation (8). Because of the phase errors discussed earlier, we used only the magnitudes of the observed visibilities, setting $F_{obs} = |V_k|$ for the k^{th} channel. The results are given in Table 3 for the first four channels; the fitted parameters were insignificant on the other channels when compared with their standard errors, indicating that the polarized component has been resolved below the detection limit. Variation

Table 3

VISIBILITY VS. CML: LEAST SQUARES FITS

F_0 and A_0 are in flux units, normalized to 4.04 AU. λ_0' in degrees of System III (1967.0) longitude. Numbers in parentheses are formal standard deviations. The meridian spatial frequency of each baseline is noted.

	Hour Angle Range			
	All	$(-2.0^h, -1.0^h)$	$(-1.0^h, +0.5^h)$	$(+0.5^h, +2.0^h)$
Channel 1A $(253'')^{-1}$				
F_0	23.62(.06)	23.94(.13)	23.19(.10)	23.78(.08)
A	0.53(.08)	0.92(.18)	0.55(.14)	0.41(.11)
λ_0'	227(8)	211(11)	229(14)	256(15)
Channel 1B $(253'')^{-1}$				
F_0	24.11(.08)	22.69(.17)	24.42(.14)	24.79(.09)
A	0.62(.11)	0.52(.24)	0.68(.16)	0.47(.13)
λ_0'	204(10)	191(24)	191(13)	212(15)
Channel 2 $(126'')^{-1}$				
F_0	21.58(.14)	20.31(.14)	21.57(.11)	22.38(.09)
A	.26(.10)	.53(.20)	.66(.16)	.32(.13)
λ_0'	297(21)	261(20)	316(13)	89(22)
Channel 3 $(84'')^{-1}$				
F_0	17.69(.06)	17.44(.10)	17.02(.10)	18.32(.08)
A	.15(.08)	.25(.15)	.29(.14)	.11(.11)
λ_0'	169(27)	247(30)	174(26)	9(45)

of Jupiter's distance during the observations was accounted for by normalizing the data to the standard distance of 4.04 AU. To check for consistency, we also partitioned the data into three hour-angle ranges and computed the parameters separately for each; note also that Channels 1A and 1B have the same baseline.

Only on the closest-spacing interferometers, Channels 1A and 1B, do we see significant polarized flux. Our best estimates of the corresponding parameters are $A = 0.58 \pm 0.2$ f.u. and $\lambda_0' = 216^\circ \pm 25^\circ$ (System III, 1967.0 longitude), where the error estimates are peak errors based on the redundant baseline and hour angle partitioning. Table 4 summarizes these results, and also gives estimates of the polarized flux density F_1; the latter were obtained using equation (9) with $\alpha = 10^\circ$ (radio astronomical value, e.g. Whiteoak et al. 1969) and $\alpha = 15^\circ$ (Pioneer 10 value). Values of F_1 are lower limits to the total synchrotron flux, and are consistent with the upper limits to the non-disk flux derived earlier from studying the residuals of the best-fit disk.

It should be noted that our value of λ_0, the Jovian longitude of the northern-hemisphere magnetic pole, is in disagreement with values obtained by others. Table 5 compares the various results which have been reported. We have been unable to find any instrumental effects to which to attribute the discrepancy.

On the other hand, there are several reasons to think that the simple model of equation (7) is not correct. First, it does not include the known beaming of the emission in the magnetic equatorial plane; but because the

Table 4

POLARIZED FLUX RESULTS

F_0, unpolarized flux	23.8 ±.7 f.u.*
$\lambda_0 = \lambda_0' - 90^\circ$, longitude of pole, System III (1967.0)	126° $\pm 25^\circ$
A, amplitude of first harmonic	0.58 ±0.2 f.u.*
F_1, estimate of polarized flux assuming $\alpha = 10^\circ$	3.20 ±1.1 f.u.*
F_1, assuming $\alpha = 15^\circ$	2.19 ± .75 f.u.*

*Normalized to the standard distance of 4.04 AU.

Jovicentric declination of the earth was very small during 1973 ($|D_E| < 0.5^\circ$), this should have little effect on the computed value of λ_0. More importantly, however, there may be pronounced asymmetries in the radiation belts, perhaps due to magnetic field anomolies. There is evidence for this from linear polarization measurements at 21 cm, 11 cm (Roberts and Komesaroff 1965), and 6 cm (Whiteoak et al. 1969); and from synthesis maps at 21 cm (Branson 1968). If such asymmetries are more pronounced at 2.8 cm, or if they are time-varying, they could explain the apparent discrepancy in Table 5.

Table 5

PUBLISHED DETERMINATIONS OF λ_0

Reference	Method	Epoch of Observation	Value(λ_0^{III} 1967)
Bash et al. 1964	Lin. pol. at 10 cm	1962.9	200.7° $\pm 2.4^\circ$
Roberts & Komesaroff 1965	Lin. pol., 21 cm & 11 cm	1962.5 1963.8	202.0 ±4.
Branson 1968	Interferometry, 21 cm	1967.3	189.0 ±2.
Whiteoak et al. 1969	Lin. pol., 6 cm	1968.5	196.8 ±1.9
Komesaroff et al. 1970	Circular pol., 21 cm	1966.9	206.3 ±6.9
Gulkis et al. 1973	Total flux, 13 cm	1969.3 1971.45	192.2 174.9
Smith et al. 1974	Pioneer 10 magnetometer	1973.9	196.0 ±8
This report	Lin. pol., 2.8 cm	1973.8	126.0 ±25

4.6. PHASE ROUNDING

Subtraction of the best fit uniform disk response from the measured brightness cannot be justified rigorously; however, at the resolution available it is probably a reasonable approach. The indication that phase errors are the primary cause of our inability to obtain a satisfactory map of non-thermal radiation suggests the following data analysis technique. We assume a priori that the source is perfectly symmetrical; therefore, the phases of all measured visibilities should be 0 or π radians. By first rounding all measured phases to the closer of these two values, we can again apply the disk subtraction technique in attempting to map the non-disk emission. This approach is similar to amplitude interferometry with a crude

measurement of visibility phase. It is emphasized that the phase rounding operation has even less rigorous justification than does disk subtraction, and it may discard useful phase information. Accordingly, considerable caution is required in interpretation of these results.

Phase rounding was performed on data taken during the daily observations. Parameters of the best fit disk are shown in Table 6. The center offset of the disk is forced to be zero by the phase rounding so only the disk temperature and semidiameter are tabulated. Both parameters are largely invariant to the phase rounding operation indicating that temperature and semidiameter are accurately determined in spite of phase errors.

Figure 15 is a plot of the line-integrated brightness computed from the residual visibilities after subtracting the best fit disk from the phase-rounded data: as in Figs. 7 and 13, all the data from the daily observations were used. The even symmetry of the plot is a consequence of phase rounding. Excess emission is observed to peak at a distance of 1.5 R_J.

Table 6

BEST FIT DISK PARAMETERS AFTER PHASE ROUNDING (DAILY AVERAGES)

Day	1.063 ; r_p	R_{fit}	T_{fit}
73.288	20.38″	20.47″	170.3 K
73.289	20.31	20.53	172.0
73.290	20.25	20.13	158.7
73.291	20.19	20.37	164.5
73.292	20.12	20.16	156.8
73.293	20.06	20.10	170.5
73.294	20.00	20.03	163.4
73.296	19.87	20.00	165.3
73.297	19.80	19.86	166.3
73.298	19.74	19.58	161.1
73.299	19.68	19.63	163.4
73.300	19.62	19.54	163.4
73.301	19.56	19.78	166.2
73.302	19.50	19.78	166.5
73.303	19.44	19.74	169.3
73.304	19.38	19.56	168.4
73.305	19.33	19.57	165.0

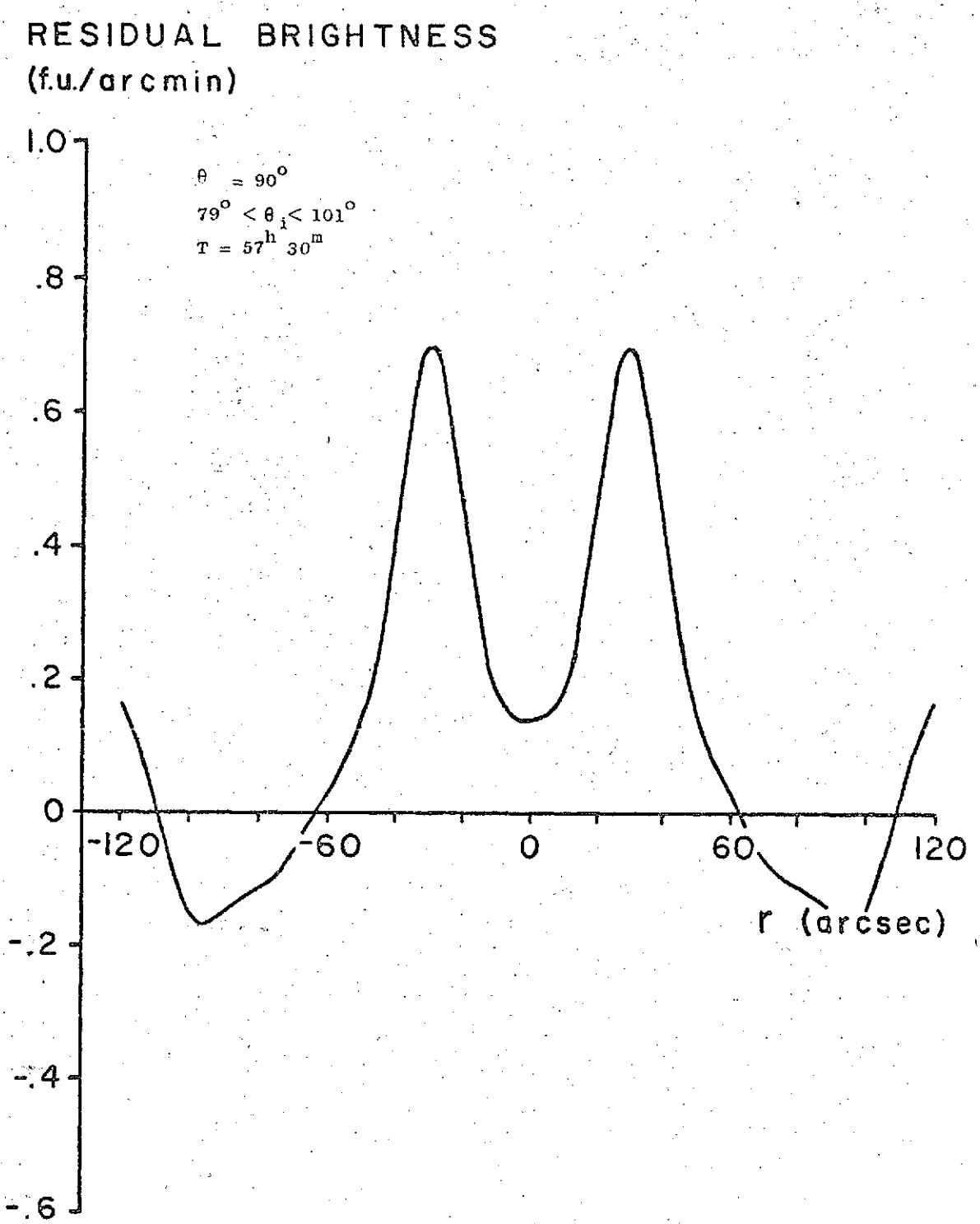

FIG. 15. Residual brightness after phase rounding and subtraction of the best-fit disk, using all data from the daily program. The even symmetry is forced by the phase-rounding operation.

5. CONCLUSIONS

Thermal emission from Jupiter has been studied by assuming that it arises from a uniformly bright disk with a temperature, semi-diameter, and center position determined by a least squares fit to the measured visibilities. These model parameters indicate a disk temperature of 160 ±10 K, a semi-diameter within 1″ of that expected from the size of the optical disk, and a center position within 1″ of the centroid of the optical disk.

Several techniques have been used to study non-thermal emission. From the absence of significant residuals after subtracting the best fit disk visibilities from the measured ones, we can place an upper bound on the strength of this component. If the non-thermal emission arises from a broad radiation belt, its strength must be less than 4.4 f.u. (4.04 AU). If the emission comes from compact regions around $1.8R_J$, it must have a flux density less than 2.9 f.u.

Variations in visibility amplitudes with CML can be used to estimate the strength of the linearly polarized component, and hence to lower bound the strength of the synchrotron component. This lower bound depends on the angular offset between magnetic and rotation axes: assuming the radio astronomy value of 10°, the lower bound is 3.2 ±1.1 f.u.; with the Pioneer measurement of 15°, this figure becomes 2.2 ±.7 f.u. This analysis also indicates the CML of the northern hemisphere magnetic pole to be 126° $\pm 25^{\circ}$ (System III, 1967.0).

After subtracting the best fit disk visibilities from the measured ones, we attempted to map the residual brightness due, presumably, to non-thermal mechanisms. Owing to the sensitivity of this process to small

instrumental calibration errors, this exercise proved unsatisfactory. With the additional assumption that the total source structure is symmetric, we produced plots of line-integrated residual brightness which peak at approximately $1.5R_J$. The technique used cannot be justified rigorously, and confirmation of this value will require additional observations after more accurate calibration.

Recent improvements to the Stanford interferometer should make these future observations fruitful. Most important is the installation of low-noise mixers which have reduced the system noise temperature to 400 K. This improvement will permit more accurate calibration of the instrument in addition to increased sensitivity to the non-disk component. Improvements in calibration at Jupiter's declination will allow more accurate mapping of non-disk emission.

Also, installation of remote feed horn rotators is now complete. This system permits us to make a careful study of the polarization properties of Jovain emission. Particularly attractive is the possibility of observations with crossed feeds to eliminate the randomly polarized thermal component.

References

Bash, F.N., F.D. Drake, F. Gundermann, C.E. Heiles, 1964, "10 cm Observations of Jupiter," Ap. J. 139, 975.

Berge, G.L., 1966, "An Interferometric Study of Jupiter's Decimetric Radio Emission," Ap. J. 146, 767.

Bracewell, R.N., R.S. Colvin, L.R. D'Addario, C.J. Grebenkemper, K.M. Price, and A.R. Thompson, 1973, "The Stanford Five-Element Radio Telescope," Proc. IEEE, Special Issue on Radio Astronomy 61, 1249.

Branson, N.B.A., 1968, "High Resolution Radio Observations of the Planet Jupiter," M.N.R.A.S. 139, 155.

Brice, N.M., and G.A. Ioannidis, 1970, "The Magnetospheres of Jupiter and Earth," Icarus 13, 173.

Brice, N.M., and T.R. McDonough, 1973, "Jupiter's Radiation Belts," Icarus 18, 206.

Carr, T.D., 1971, "Jupiter's Magnetospheric Rotation Period," Ap.L. 7, 157.

Carr, T.D., and S. Gulkis, 1969, "The Magnetosphere of Jupiter," ARAA 7, 577.

D'Addario, L.R., 1974, "The Stanford Synthesis Radio Telescope: Theory, Calibration, and Data Processing; and a Study of Galactic H II Regions," Ph.D. dissertation, Stanford University, Chapter 5.

Dickel, J.R., J.J. Degioanni, G.C. Goodman, 1970, "The Microwave Spectrum of Jupiter," Radio Science 5, 517.

Gulkis, S., and B. Gary, 1971, "Circular Polarization and Total Flux Measurement of Jupiter at 13.1 cm Wavelength," AJ 76, 12.

Gulkis, S., B. Gary, M. Klein, and C. Stelzried, 1973, "Observations of Jupiter at 13 cm Wavelength during 1969 and 1971," Icarus 18, 181.

Klein, M.J., and S. Gulkis, 1974, "The Location of Jupiter's Magnetic Dipole," presented at AAS Division of Planetary Sciences Meeting, Palo Alto, Calif., 3 April 1974.

Komesaroff, M.M., D. Morris, J.A. Roberts, 1970, "Circular Polarization of Jupiter's Decimetric Emission and the Jovian Magnetic Field Strength," Ap.L. 7, 31.

Moffet, A.T., 1968, "Minimum Redundancy Linear Arrays," IEEE Trans. on Antennas and Propagation, AP-16, 172.

Price, K.M., 1973, "Array Pointing Function," Stanford Radio Astronomy Institute Glint No. 507.

Roberts, J.A., and M.M. Komesaroff, 1965, "Observations of Jupiter's Radio Spectrum and Polarization in the Range from 6 cm to 100 cm," Icarus 4, 127.

Ryle, M., 1962, "The New Cambridge Radiotelescope," Nature 194, 517.

Smith, E.J., L. Davis, Jr., D.E. Jones, D.S. Colburn, P.J. Coleman, Jr., P. Dyal, and C.P. Sonett, 1974, "The Magnetic Field of Jupiter and Its Interaction with the Solar Wind," Science 183, 305.

Warwick, J.W., 1970, "Particles and Fields Near Jupiter," NASA Contractor Report CR-1685.

Wernecke, S.J., 1973, "Full Sky Phase Calibration - Winter 1973," Stanford Radio Astronomy Institute Glint No. 519.

Whiteoak, J.B., F. F. Gardner, and D. Morris, 1969, "Jovian Linear Polarization at 6 cm Wavelength," Ap.L. 3, 81.